Seismic Evidence for Fluid/Gas Beneath the Mentawai Fore-Arc Basin, Central Sumatra

Gabriel Huot, Satish C. Singh

AGU PUBLICATIONS

JGR

Journal of Geophysical Research: Solid Earth

RESEARCH ARTICLE
10.1002/2017JB014849

Key Points:
- Full waveform inversion was used on streamer data from Sumatra forearc basin
- A low velocity zone is highlighted above the backthrust
- Mud volcanism might be generated by mobilization of local and deep fluids

Supporting Information:
- Supporting Information S1

Correspondence to:
G. Huot,
huot@ipgp.fr

Citation:
Huot, G., & Singh, S. C. (2018). Seismic evidence for fluid/gas beneath the Mentawai forearc basin, Central Sumatra. *Journal of Geophysical Research: Solid Earth*, *123*, 957–976. https://doi.org/10.1002/2017JB014849

Received 11 AUG 2017
Accepted 19 JAN 2018
Accepted article online 25 JAN 2018
Published online 12 FEB 2018

Seismic Evidence for Fluid/Gas Beneath the Mentawai Fore-Arc Basin, Central Sumatra

Gabriel Huot[1] **and Satish C. Singh**[1]

[1] Laboratoire de Géosciences Marines, Institut de Physique du Globe de Paris, Paris, France

Abstract Since 2004, there have been three great interplate earthquakes (Mw > 8.0) offshore Sumatra. In addition to rupturing the megathrust, these earthquakes might also have ruptured the backthrusts that bound the Andaman Islands to the Mentawai Islands toward the forearc basins. Here we apply a combination of traveltime tomography and seismic full waveform inversion to an ultralong offset seismic reflection profile from the Mentawai forearc basin, in the region of the 2007 Mw 8.4 Bengkulu earthquake. We perform a waveform inversion of far-offset data followed by a waveform inversion of near-offset data using the starting model derived from the traveltime tomography. Our results show the presence of a large, low-velocity anomaly above the backthrust. The seismic reflection image indicates that this low-velocity anomaly lies either within highly compacted sediments from the accretionary wedge or within highly deformed sediments from the forearc basin. The porosity estimation, using the effective medium theory, suggests that a small amount of gas (from 2 to 13%) or a significant amount of fluid (from 17 to 40%) could generate this low-velocity zone. The presence of fluids and the observation of bottom simulating reflector below a push-up ridge might be associated with mud diapirism. The fluids could originate locally from the dewatering of the sediments from the accretionary wedge or forearc basin. The high reflectivity of the backthrust in this region might also indicate deeper fluid origin, either from underplated sediments on the subduction interface or from the serpentinized mantle wedge.

Plain Language Summary Earthquakes, occurring in plate convergence areas (subduction zone), can generate destructive tsunamis. The power of these tsunamis is not necessarily related to the magnitude of associated earthquakes. Therefore, understanding the mechanisms and processes that influence earthquakes is critical if we want one day to prevent efficiently the risks. Sumatra is one of the most active zones of Earth. Seismic data were recorded on sea to image structures below the seafloor in the Mentawai forearc basin, between Sumatran Islands and Sumatran main land, in the region of the powerful 2007 and 2010 earthquakes. We found evidences of fluid/gas below the seafloor. Fluid and gas in forearcs are related to flux from within the basin or could also be associated to deep fluid release from the subduction interface. Fluids are an important parameter that influences earthquake rupture. At the moment, more data would be needed to understand the exact origin of these fluids. Understanding of fluid flux could make it possible to identify areas where powerful tsunamis can be generated.

1. Introduction

The Sumatra subduction zone experienced three great interplate earthquakes (moment magnitude Mw > 8.0) since the beginning of the 21st century. The most destructive was the December 2004 Sumatra-Andaman Mw 9.2 earthquake, which was one of the most powerful earthquakes recorded on Earth. This earthquake generated a tsunami that took more than 230,000 lives in countries around the Indian Ocean. This event was followed by the March 2005 Nias-Simeulue Mw 8.7 earthquake, which broke 350 km of plate boundary farther southeast and initiated at 30 km depth (Briggs et al., 2006). About 1,300 km southeast from the 2004 event, in the Mentawai region, a set of twin earthquakes of Mw 8.4 and 7.9 occurred in 2007 (Figure 1) at depths of 20 and 43 km, respectively (Konca et al., 2008). A gap of 600 km still remains between the 2005 and 2007 great earthquakes. Although the 2005 and 2007 events had high moment magnitudes, no significant tsunami were generated.

Before the 2004 event, the analysis of historical records (Newcomb & McCann, 1987) and coral stratigraphy (Natawidjaja et al., 2006) show that only three great earthquakes occurred during the past 300 years, rupturing

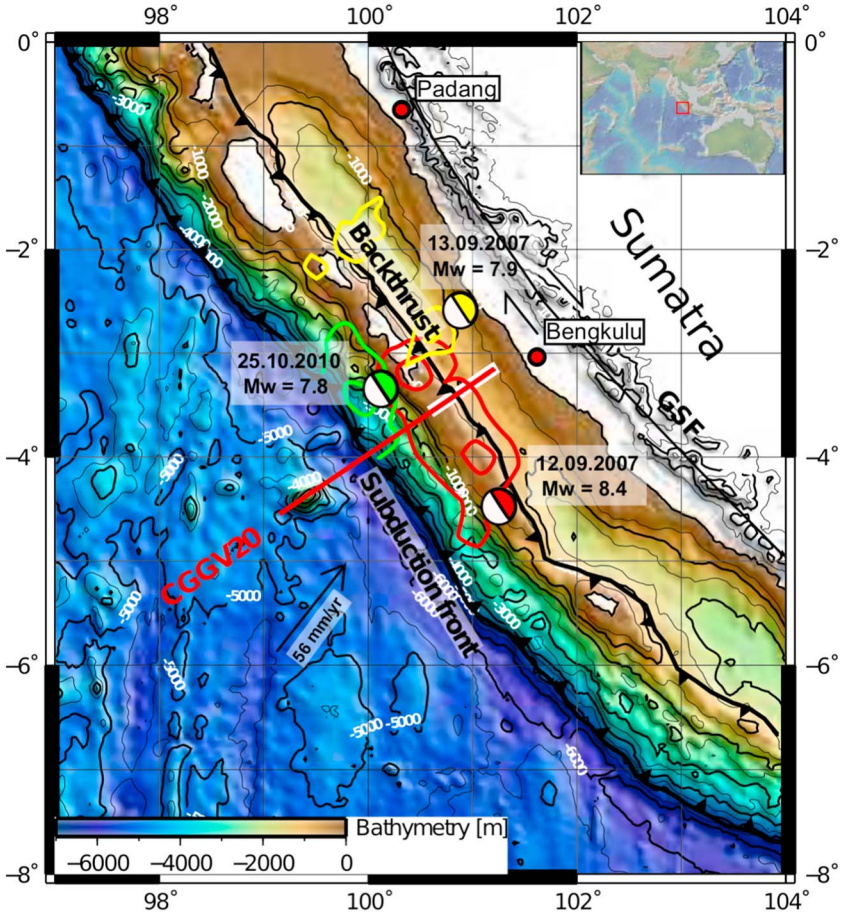

Figure 1. Location map of the study area. The black thick line indicates the backthrust and the black thin line indicates the Great Sumatra Fault (GSF) (Singh et al., 2010). Beach balls and contour lines correspond to the main earthquakes and corresponding ruptured areas. Red line is the CGGV20 profile and the white line behind indicates the part of the data used in this study. The profile CGGV20 was acquired in central Sumatra, across the Mentawai forearc. The location of the map is shown in the insert at the right-hand corner.

the megathrust in the forearc region. The 1861 great earthquake ruptured the same forearc region as the 2005 event (Natawidjaja et al., 2006). The 1797 and 1833 great earthquakes ruptured the Mentawai segment, including the 2007 rupture zone and the northern locked region (Newcomb & McCann, 1987). The recent 2005 and 2007 ruptures suggest that the locked segment, which previously ruptured in 1797, could produce a great earthquake in the near future.

Singh et al. (2010) demonstrated the existence of an important fault system in the Sumatran forearc, the Mentawai Fault Zone (MFZ), acting as a seaward dipping backthrust. The Mentawai backthrust seems to have been reactivated after at least 30 years of inactivity (Wiseman et al., 2011). A cluster of seismic events started after the 2005 Nias-Simeulue great earthquake, with another in 2009. Although the recent earthquakes have moderate magnitude (< Mw 6.5), Wiseman et al. (2011) suggested that an earthquake of magnitude Mw 7.9 to 8.5 could occur along the backthrust. It has also been suggested that the backthrust could rupture coseismically during a great earthquake, such as during the 2004 and 2007 earthquakes (Chauhan et al., 2009; Singh et al., 2011). Simultaneous rupture of the backthrust along with the megathrust could increase the tsunami risk in central Sumatra. However, geological records suggest that the activity of the Mentawai is decreasing and that the current slip rate is small, 1 mm/yr (Mukti et al., 2012). Hence, the immediate risk of a large earthquake and associated tsunami should be small (Mukti et al., 2012). Based on the enhanced reflectivity of the backthrust in the 2007 earthquake rupture zone, Singh et al. (2011) suggested that the backthrust might have been reactivated during the 2007 earthquake, coseismically or afterward, and suggested that this might be due to the presence of fluids derived from the mantle wedge. However, based simply on reflectivity, it is not possible to rule out the possibility of high lithological contrast between the highly compacted sediments

from the accretionary wedge and the continental crust. Mylonite and anisotropy could also generate an enhanced reflectivity, but this possibility is unlikely (e.g., Fountain et al., 1984) due to the low temperature and pressure profile of backthrusts, and the strong reflective nature of the reflector from the forearc basin to the subduction interface.

In this paper, we investigate the seismic properties of the backthrust in the 2007 rupture zone. We apply a combination of traveltime tomography (TTT) and elastic Full Waveform Inversion (FWI) to ultralong offset streamer data from the 2007 earthquake rupture zone (Singh et al., 2011) to retrieve the detailed velocity structure of the forearc basin, and correlate it to the seismic imaging. Finally, we use the effective medium theory (EMT) to shed light on the fluid presence and discuss its origin.

2. Background

In the Sumatra subduction zone, the Indo-Australian plate subducts beneath the Sunda plate obliquely, with a convergence rate varying from 60 mm/yr in the south to 52 mm/yr in the north (Prawirodirdjo & Bock, 2004). The dextral component of the relative motion between the two plates is accommodated by a trench-parallel strike-slip fault system (Fitch, 1972). The Great Sumatran Fault (GSF), located 300 km from the trench, lies within the volcanic arc and has been shown to accommodate most of this motion with decreasing slip rates from north to south (Bellier et al., 1999; McCaffrey et al., 2000; Sieh & Natawidjaja, 2000). The MFZ, which cuts through the forearc basin, was first interpreted as a strike slip fault accommodating additional strike-slip motion (Diament et al., 1992; Kopp et al., 2001; Schlüter et al., 2002). However, high-resolution seismic reflection and bathymetric data showed that the MFZ is actually a seaward-dipping backthrust (Singh et al., 2010).

The age of the subducting plate varies from 40 Ma to 80 Ma (Muller et al., 2008), with the youngest oceanic crust subducting east of Nias Island in northern Sumatra. The age and convergence rate of subduction are two important parameters controlling the thermal regime of the subduction and are used in global thermal modeling to predict the depths where dehydration reactions occur in the subducting slab (van Keken et al., 2011). Sediment thickness in central Sumatra is low, up to 1.5 km at the deformation front, from which 40% (0.6 km) are estimated to be subducted (Syracuse et al., 2010). A temperature of ~200°C is predicted on the slab surface at 30 km depth in Sumatra (Syracuse et al., 2010; van Keken et al., 2011), enabling dehydration below the forearc mantle. Collings et al. (2012) identified a low velocity at the forearc mantle wedge in the Mentawai region (30 km depth), indicating a moderate hydration of 12–14%. They suggested the possibility of fluid propagation from the mantle wedge to the backthrust based on this serpentinization and clusters of activity at the backthrust (Collings et al., 2012). Water flux is a key parameter that influences the coupling and seismogenic behavior of the megathrust and could be an indicator of fault activity in the forearc (Singh et al., 2011).

The Andaman-Sumatra subduction system is unique: the accretionary wedge is up to 180 km wide, dotted with subaerial forearc high islands, and a wide forearc basin (McNeill & Henstock, 2014). The Mentawai section of the Sumatran subduction has a 100 km wide and 800 km long forearc basin containing 3 to 7 km of sediments (Mukti et al., 2012). This basin lies between mainland Sumatra and the forearc high. Forearc high islands have developed due to the subareal emergence of accretionary wedge sediments. Seaward vergent thrusts have been identified in the forearc high both inland (Amin et al., 1993; Andi Mangga et al., 1994; Budhitrisna & Andi Mangga, 1990) and offshore (Mukti et al., 2012). A mélange complex is present inland along these thrusts (Andi Mangga et al., 1994; Budhitrisna & Andi Mangga, 1990) and is inferred to be related to ancient mud diapirs and mud volcanoes (Barber, 2013; Samuel & Harbury, 1996). Landward of the forearc high islands, the Mentawai forearc basin is a depocenter of marine and lacustrine sediments since the late Eocene (Hall et al., 1993). The inner wedge of the forearc basin is deformed by a landward-vergent high-angle backthrust that corresponds to the MFZ (Mukti et al., 2012). Active mud volcanoes have been identified along the MFZ, contributing to the active deformation (Mukti et al., 2012; Samuel & Harbury, 1996).

Our study area lies southwest of mainland Sumatra, where the 2007 Mw 8.4 Bengkulu earthquake occurred (Figure 1). The seismic line CGGV20 crosses the forearc basin in the shallower part of the Mentawai basin where the water depth is around 800 m. The water depth on the forearc high is 50 m. Seismic time image (Figure 2a) shows 5 s two-way traveltime (TWT) thick sediments (~ 6–7 km) above a strong landward vergent reflector at 6 s TWT. This reflector is interpreted as the continental backstop for accretionary wedge development

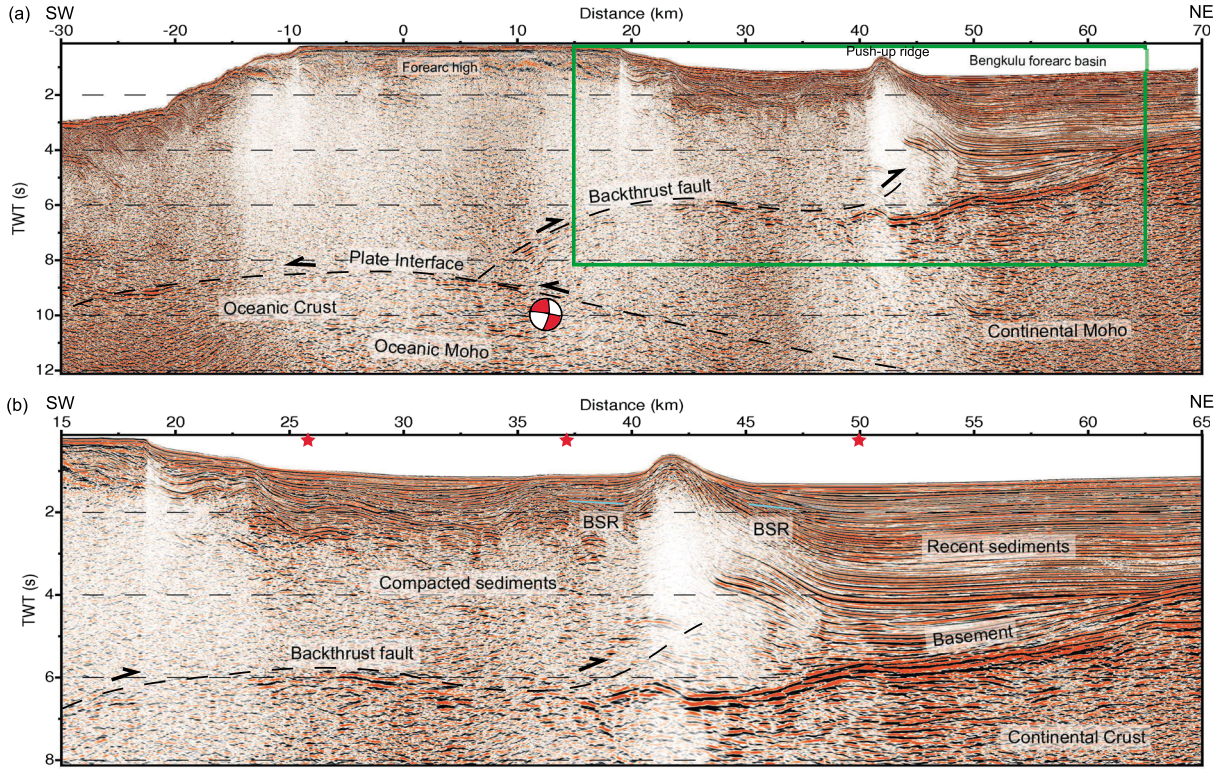

Figure 2. Poststack time migrated seismic image of profile CGGV20. (a) The beach ball corresponds to the projected location of the 2007 earthquake. The green rectangle corresponds to the blow up shown in Figure 2b. (b) Blow up of the seismic image of the forearc basin for which the inversion was performed. Light blue lines correspond to bottom-simulating reflectors (BSRs). Dashed black line corresponds to the backthrust. Red stars are the locations of shot gathers shown on Figure 3.

(Kopp & Kukowski, 2003; Mukti et al., 2012). The backstop is represented by a strong reflection, separating forearc basin sediments and older sediments or basement rock. Further SW, following the basement, the backthrust has high reflectivity and can be followed down to the subducting plate at 9 s TWT. A push-up ridge is visible at 45 km on the profile. This anticlinal ridge has 500 m of relief and is 3 km wide. The deformation beneath the ridge is interpreted as folding and faulting. The absence of reflectivity suggests that the sediments southwest and beneath the push-up ridge could be highly deformed or compacted, similarly to the forearc high sediments (Figure 2b). Mud diapirism or mud volcanism could have disturbed the folds and thrusts (Mukti et al., 2012). The presence of bottom simulating reflectors (BSRs) on both sides of the push-up ridge, between 1.5 and 2 s TWT, is interpreted as gas hydrate reflections, indicating the existence of free gas in the region (Singh et al., 1993). Gas hydrates are often linked to deep-water mud volcanoes or diapirs (Milkov, 2000). Sediments are well imaged northeast (NE) of the push-up ridge, from the seafloor to the basement. Deformation by folding is extensive close to the push-up ridge, affecting strata from the basement to 300 ms TWT below the seafloor. The deformation is localized and did not affect the sediments of the same strata farther NE. Southwest (SW) of the push-up ridge, only 2 s TWT thick sediments, which are highly folded, can be seen above the nonreflective sediments.

3. Seismic Data

3.1. Acquisition and Processing

The deep seismic reflection data were acquired by CGG in May 2009 on board the seismic vessel *Geowave Champion* using a 15 km ultralong streamer towed at 22.5 m depth, and two 6 km long streamers towed at 7.5 m and 15 m depth. An array of air guns with a total volume of 9,600 cubic inches, deployed at 15 m depth, was used as the seismic source (Singh et al., 2009). The shot spacing was 50 m, the group spacing 12.5 m and the record length 20 s. The distance between the shot array and the closest channel was 125 m. The deep seismic profile CGGV20 is about 260 km long and was recorded from NE to SW. It covers the area from the NE edge of the forearc basin, passing through the forearc high, then farther seaward down to the trench

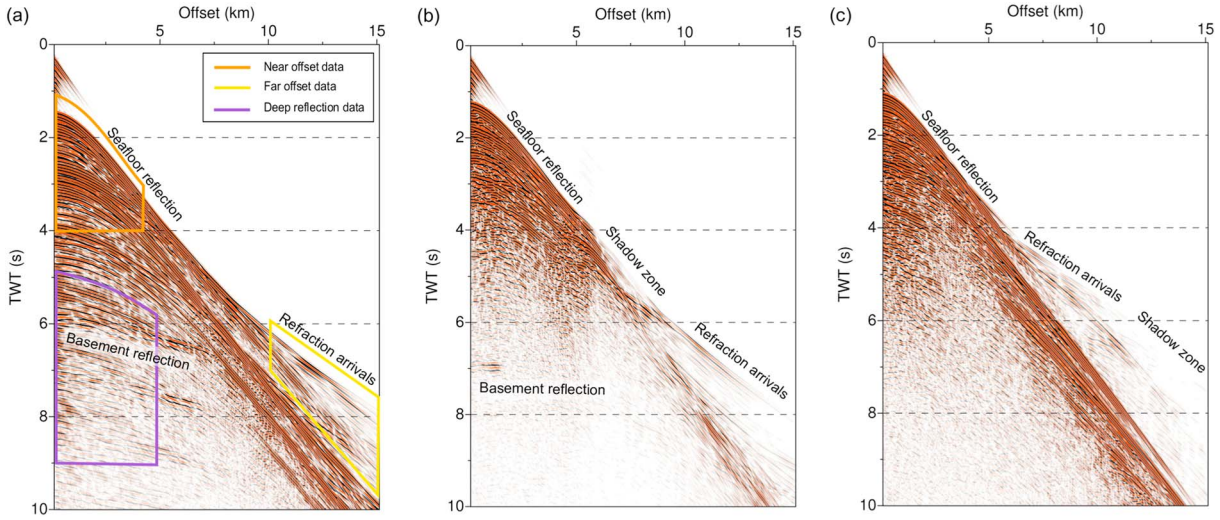

Figure 3. Shot gathers at three different locations. Principal wave arrivals are annotated on the figures. The zero offset corresponds to the position of the shot array. (a) The shot is at 50 km distance and the receivers above the thick sediments. Windowing of the data for the FWI: Yellow polygon: Step 1, Orange polygon: Step 2, and Purple polygon: step 3. (b) The shot is at 37 km distance and the receivers above the push up ridge. (c) The shot is at 26 km distance and the receivers above compacted sediments.

and ending SW of a huge seamount (Figure 1). We focused our study on the forearc basin part of the profile, choosing 80 km of data that correspond to 1,298 shots. For the TTT, the full model was inverted. We show only reliable results from 15 to 65 km distance corresponding to the full fold. For the FWI, we inverted from 20 to 80 km distance range due to the complexity of the inversion in the shallow water of the forearc high (between 0 and 20 km distance range). The velocity model from 15 to 20 km distance range is identical in the TTT and FWI models.

3.2. Preprocessing for the FWI

Low frequencies are critical to properly invert for long and possibly intermediate wavelengths (Sirgue, 2006). We used a combination of high-pass filter to remove signal and strong noise due to swell below 1 Hz and F-K filter to only remove the noise over 1 Hz. To apply the frequency continuation strategy (Bunks et al., 1995), we processed independently the data with three different low-pass filters at 6, 9, and 12 Hz maximum frequency. Due to finite difference modeling scheme, 12 Hz was the maximum frequency that could be modeled with 1.5 ms resampled data (Levander, 1988). Of the 20 s recording length, only 10 s of data were used, containing the main features of the forearc basin. This was necessary to reduce computation time and decrease the memory requirement. The receivers were finally decimated to 25 m spacing instead of 12.5 m to match the model grid point interval of 25 m. Hence, the resulting shot gathers were formed of 600 traces.

Since we use a two-dimensional (2-D) elastic FWI and aim for inverting amplitudes, we compensated the amplitude and phase of the data by applying a 3-D to 2-D transformation. The data were multiplied by $\sqrt{t}$ to compensate for the geometrical spreading and convolved with $\frac{1}{\sqrt{t}}$ to correct the phase (Pica et al., 1990). Although this simple transformation is mainly valid for a 1-D velocity, it sufficiently mitigates differences between observed and synthetic data (e.g., Arnulf et al., 2012; Wang et al., 2015).

3.3. Data Description

We use refraction arrivals for TTT and full waveform inversion first. Figure 3 shows three shot gathers from NE to SW on the profile (Figure 2b). On the shot gather where the recent sediments are thick (Figure 3a), high-energy reflections are visible down to more than 8 s TWT, and the refraction arrivals have high amplitudes from 7 to 15 km. Around the push-up ridge (Figure 3b), high energy reflections are only visible down to 3.5 s TWT. A reflected arrival can be seen at 7 s TWT corresponding to the basement reflection. The refraction arrivals are weaker than in the area of thick sediments (Figure 3a). A shadow zone seems to be present between 5.5 and 8.2 km offset range, followed by higher apparent velocity at farther offsets. Close to the forearc high in the area of poor reflectivity (Figure 3c), high amplitude reflections can be seen down to 3 s TWT. From 6 km offset, a high apparent velocity refracted arrival can be observed, followed by a shadow zone from 11 km offset, which corresponds to weak amplitude signal with lower apparent velocity than other shot gather

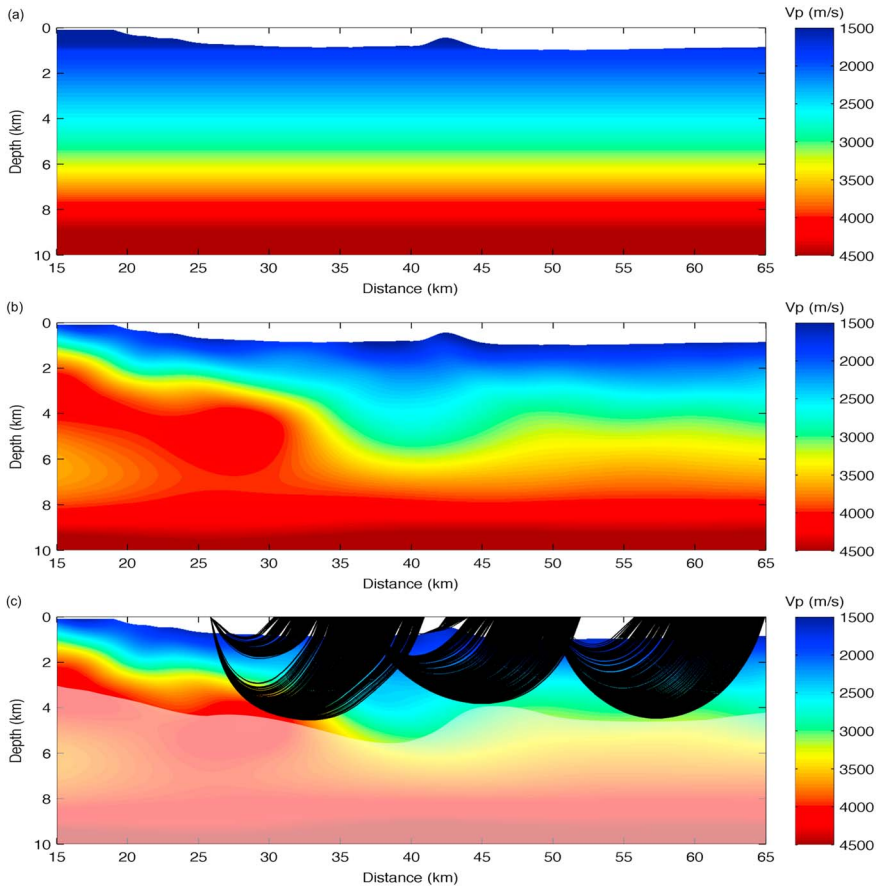

Figure 4. Tomographic inversion, model A. (a) Initial V_p model. (b) Final V_p model. (c) Ray diagram of the three shot gathers shown in Figure 3. The slightly whitened area is below the ray coverage.

(Figures 3a and 3b) at far offset. The complexity of this shot gather indicates a significant lateral variation in velocity in this region with decreasing velocities northeastward.

4. TTT

4.1. Methodology

We performed TTT to retrieve an accurate and smooth starting velocity model required for FWI (Virieux & Operto, 2009). TTT consists of inverting first-arrival picked traveltimes of shot gathers to retrieve a *P* wave (V_p) velocity model. The algorithm used for this study is an updated version of Van Avendonk et al. (2004) (Arnulf et al., 2014; Jian et al., 2012). As starting model for the TTT, we used a 1-D starting velocity model, model A, corresponding to the center of the velocity model derived from CGG velocity analysis (smoothed interval velocities computed after RMS velocity from CMP gather flattening) at 40 km distance (Figure 4a). The velocity model was discretized on an 80 by 10 km box at 25 m grid spacing.

To optimize picking time and accuracy, we manually picked every fourth shot gather (200 m interval) with a flexible algorithm, which uses interpolation, hence, a total of 324 shots out of 1298. The decimation of the shots is justified by the fact that the data set is oversampled beyond the resolution of the TTT (Arnulf et al., 2014).

The traveltimes were computed by ray tracing using the shortest path method (Moser, 1991). The misfit, the difference between observed and computed data weighted by their uncertainties, is minimized in a least squares sense (Van Avendonk et al., 1998, 2004). The uncertainty in the data depends on the uncertainty in the shot and receiver locations (~2 ms), in the bathymetry (~8 ms), and in the traveltime picking (~4 ms) (Arnulf et al., 2014; Ghosal et al., 2014). Considering that the uncertainties are independent, this leads to a root-mean-square uncertainty of ~10 ms. The initial misfit was extremely high due to the choice of 1-D model

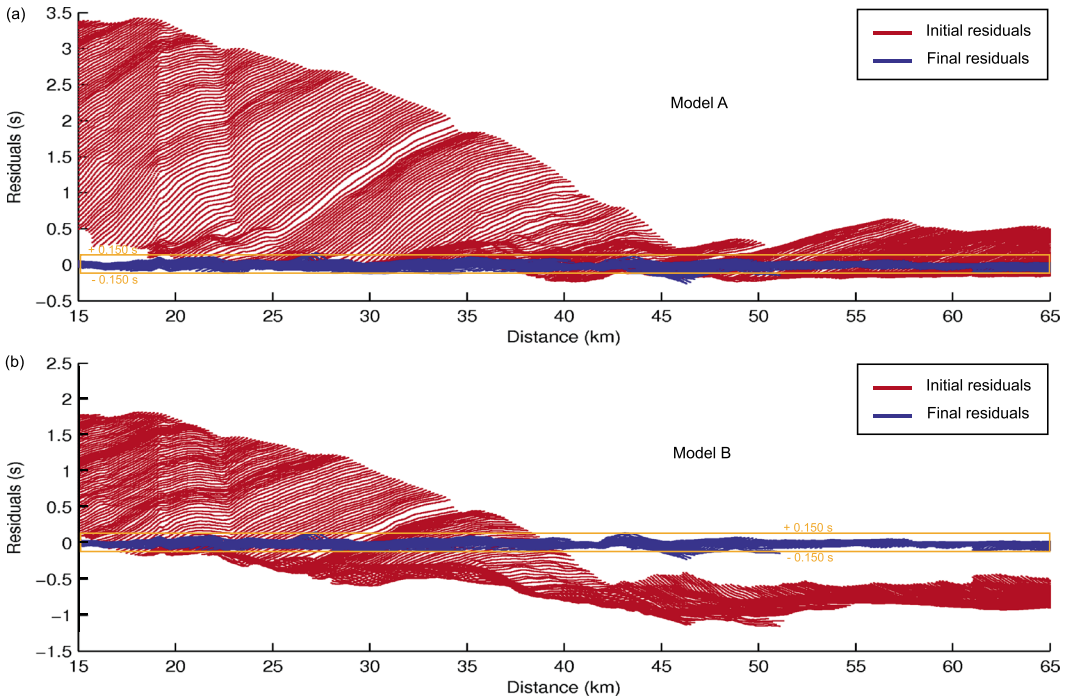

Figure 5. Initial (red) and final (blue) traveltime residuals. Residuals inside the orange rectangle are under 0.150 s. (a) Model A. (b) Model B.

(Figure 4a) as a starting model. Therefore, a strong regularization, based on a roughness matrix containing the first and second derivatives of the velocity model, was used to stabilize the inversion (Van Avendonk et al., 2004).

4.2. Results of TTT

We performed 14 iterations to obtain the final model (Figure 4b). The ray diagram in the final model shows ray coverage from 3.2 to 5.5 km depth (Figure 4c). The initial residuals for all of the offsets along the whole profile are positive (Figure 5a), suggesting that the velocity should be higher than the 1-D model with a higher velocity gradient. From 15 to 33 km distance and below 2 km depth, results highlight a high-velocity structure with a maximum velocity of 4.9 km/s. Above this structure the velocity abruptly changes to a lower-velocity structure (<3 km/s). From 33 to 45 km, results show an abrupt change from SW to NE, from high velocity (>4 km/s) to low velocity (<3 km/s) between 2 and 6 km depth. From 45 to 65 km, the velocity increases and remains fairly constant horizontally (~3 km/s at 4 km depth).

To validate the robustness of the method, we performed an inversion with a second 1-D starting model (Figure S1a in the supporting information), model B, in which we increased the velocity by 500 m/s at each grid point compared to model A (except in the water column). This high-velocity starting model converges to the same solution (Figure S1b) in the illuminated area (Figures S1c and S2). Figure S2 shows the derivative weight sum (DWS) for model A (Figure S2a) and model B (Figure S2b), and demonstrates the coherency of both inversions. The area corresponding to the low-velocity zone (LVZ) has less ray coverage due to its complexity (Figures S2a and S2b). The 15 km long offset streamer made it possible to have enough far offset data crossing this area to have consistent inversions (similar results for models A and B). Over 99% of the final residuals for both velocity models are within a range of ±0.150 s (Figure 5). The final chi-square misfits are ~10 for both models, which corresponds to a mean time residual of ~32 ms. The chi-square misfit could be decreased to 1 for the highest resolution, which would correspond to a final time residual equivalent to the assigned data error (Van Avendonk et al., 2004). However, in order to obtain a smooth model for the FWI, we kept the misfit at ~10.

Although structures imaged by the TTT are above the maximum resolution of the method (kilometer scale) for marine data (Arnulf et al., 2014; Ghosal et al., 2014), we performed a checkerboard test, perturbing the final

model A by 10 km wide and 4 km thick Gaussian anomalies (Figure S3a). The top and width of the anomalies were properly inverted, whereas there was more difficulty to invert the bottom parts (Figure S3b).

5. FWI

5.1. Methodology

FWI is a quantitative imaging technique capable of retrieving detailed Earth properties from seismic data (Lailly, 1983; Tarantola, 1984). Basic requirements for a successful application of FWI include the presence of low frequencies in the data, a wide aperture, and a reliable starting model (Sirgue, 2006). CGG data fulfill these requirements. Moreover, we removed the swell noise while preserving the low-frequency content in the data, using an appropriate preprocessing. Low frequencies and a wide aperture are necessary to resolve medium-scale features along with short-scale information. The starting model should have enough large-scale velocity features to avoid cycle skipping, such as the difference of traveltime, between the waveforms of the synthetic and observed data, does not exceed half a period. Residuals of TTT results are below 150 ms, which corresponds to the half period of 3 Hz (first main frequency used in our FWI process).

Acoustic wave propagation is commonly used for FWI, because it can be computationally inexpensive, but the Earth is by nature elastic and can also include attenuation effects and anisotropy. Here we use a time domain method for the modeling based on a staggered grid finite difference approximation to the elastic wave equation (Virieux, 1986), fourth order in space and second order in time (Levander, 1988), which includes both V_p and V_s, but we only invert for V_p. The algorithm was initially developed by Shipp and Singh (2002). Although this does not take into account attenuation and anisotropy, elastic FWI does account for amplitude versus offset (AVO) effects on V_p, and *P* and *S* wave conversion (Crase et al., 1990), which cannot be neglected at far offset in marine streamer acquisition (Barnes & Charara, 2009). Both V_s and density are linked to the V_p model by a realistic relationship (Castagna et al., 1985; Gardner et al., 1974) during the inversion. The gradient, which gives the direction of the model update, is computed by the adjoint state method (Plessix, 2006). We use the conjugate gradient method (Mora, 1987) to ensure convergence.

In a marine environment, the source is affected by free surface ghosts. In order to avoid heavy processing of the data that can damage the signal, we modeled the ghost and multiples by using the free surface and the proper acquisition geometry. To match our modeling with the observed data, the source wavelet was first estimated by deconvolution of the ghost signals, using the far-field signature provided by CGG.

The starting V_p model is the final velocity model obtained by TTT. We inverted 60 km of profile with a 50 m shot interval and 25 m receiver interval. The model consists of 3,201 by 401 grid points with 25 m spacing. Although the turning ray penetration was only 5–6 km, a 10 km depth model was chosen to image the deep reflections. The first shot is at 65 km distance and the last shot is located just before the forearc high at 20 km distance. As we did for the TTT, we only show the part of the model between 15 and 65 km distance.

Our inversion strategy consists of a multiscale frequency continuation strategy (Bunks et al., 1995) and data windowing of different phases: far offsets (including refraction arrivals and wide angle reflections), near-offset shallow reflections, and deep reflections (Figure 3a). Three frequency bandwidths were chosen for inversion, starting with the lowest at 1–6 Hz, then 1–9 Hz, and finally 1–12 Hz. Refraction phases were inverted first for each frequency range to improve the background velocity model down to a depth of 4 to 7 km (Figure 6a). The resulting model was then used as starting model for near-offset shallow and deep reflection inversion (Figure 6b).

5.2. Results of FWI

After applying FWI to far-offset arrivals (Figure 6a), the velocity model was significantly updated. The global misfit is reduced to 12% after 20 iterations for the first step (1–6 Hz). The residual (Figures S4a and S4b) shows a major update of first arrivals both in amplitude and phase, as well as a better fit for far-offset reflections. For the second (1–9 Hz) and third steps (1–12 Hz) of the FWI, 13 iterations were performed, and the misfit decreased to 37% and 54%, respectively. It should be noted that the wide-angle data contain wide-angle reflections, which have led to the inversion of layered structures in the model. The residuals on Figure S5 show that the inversion of far-offset arrivals is successful even in difficult area such as the LVZ. After applying FWI on reflection arrivals (Figure 6b), the resolution is further improved with velocity variations in the sediments, the appearance of the backthrust fault and a seaward verging fault at 3 km depth and 23 km distance. The residuals for the first frequency range 1–6 Hz is shown in Figures S4c and S4d. Since the sea floor

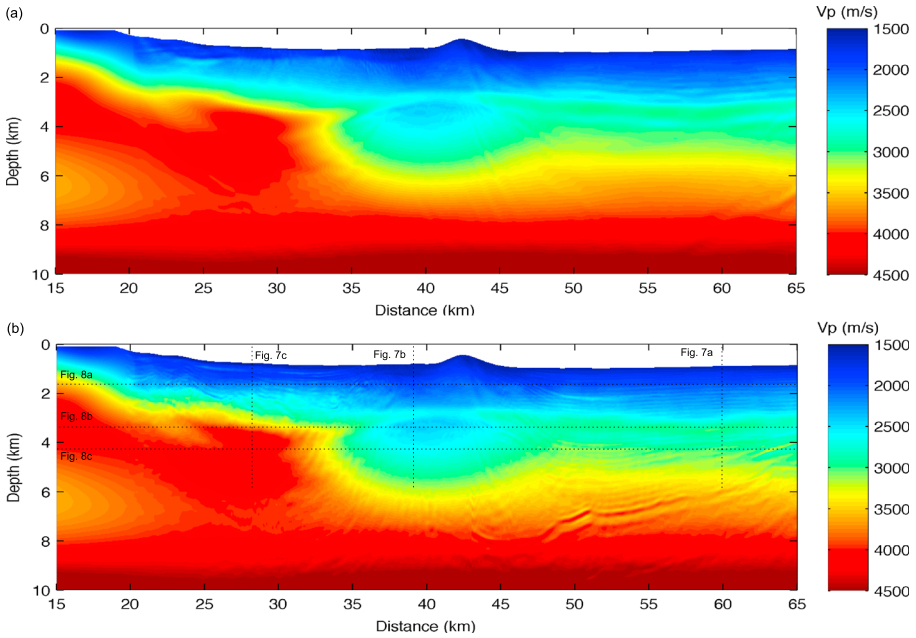

Figure 6. Updated FWI V_p models. The orange line is the maximum illumination depth. (a) Far-offset FWI V_p model. (b) Near-offset FWI V_p model. Location of horizontal and vertical 1-D plots are indicated by black dotted lines and corresponding figure numbers.

reflection was already well matched initially, the residual of seafloor reflections did not decrease. However, the FWI improved the fit for deeper reflections. Although there is no constraint of the velocity at depth, the inversion of deep reflections was then performed to image the backthrust (Figures S4e and S4f). To assess the reliability of the far-offset FWI results, we performed a checkerboard test by inverting rectangle-shaped perturbations with dimensions of 4.025 km long and 1.025 km deep (Figure S6a). Although we use refracted arrivals only to invert for these perturbations separated by a 10% sharp velocity contrast, results show that the model can be resolved up to 5–6 km depth (Figure S6b).

In the sedimented forearc basin from 45 to 65 km distance, layers with increasing velocities of 1.6 to 2.6 km/s can be observed from the seafloor down to 3.0 km depth (Figure 7a). The velocity increases abruptly to 3.1 km/s at 3.3 km depth. Then, the velocity decreases to 2.8 km/s at 3.8 km depth in a 300 m thin LVZ, which can be observed throughout the thick forearc basin (Figure 6b). Below this thin LVZ, the velocity increases linearly to 3.6 km/s at 6 km depth. Low-velocity seaward dipping layers can be observed with a 200 m/s velocity decrease (Figure 7a) compared to the background velocity, from 4 to 5.5 km depth. From 6 to 10 km depth, no reliable update can be observed because there is no ray coverage. However, we expect the velocity to increase abruptly below the continental backstop (Kopp & Kukowski, 2003).

From 33 to 45 km distance, below the southwest side of the push-up ridge, a large oval-shaped LVZ (10 km wide and 4 km thick) (Figure 6b), lies below 3 km depth. In this region, the velocity increases from 1.6 km/s at the seafloor to 2.7 km/s at 2.8 km depth (Figure 7b). Then, the velocity decreases abruptly to 2.4 km/s in the LVZ at 3.3 km depth.

Between 15 and 33 km distance, ~2.5 km of recent sediments lie above high-velocity compacted sediments from the accretionary wedge (Figure 6b). From the seafloor down to 2 km depth, layered sediments are visible and deformed by folding. Between 2 and 3 km depth, landward dipping lower-velocity layers might indicate faulting and higher deformation in older basin sediments. The velocity drop can be observed on Figure 7c at 2.6 km depth with the velocity decreasing from 2.9 to 2.6 km/s. Below 3 km depth, the velocity increases rapidly from 3.3 to 4.3 km/s, indicating highly compacted sediments from the accretionary wedge. The landward dipping velocity drop into the accretionary wedge could correspond to a forearc high thrust fault described by Mukti et al. (2012), common in the Sumatra forearc high area both inland and offshore.

There are significant horizontal velocity variations from the accretionary wedge sediments in the southwest to thick forearc basin sediments in the northeast. At 1.75 km depth (Figure 8a), the velocity has small variation

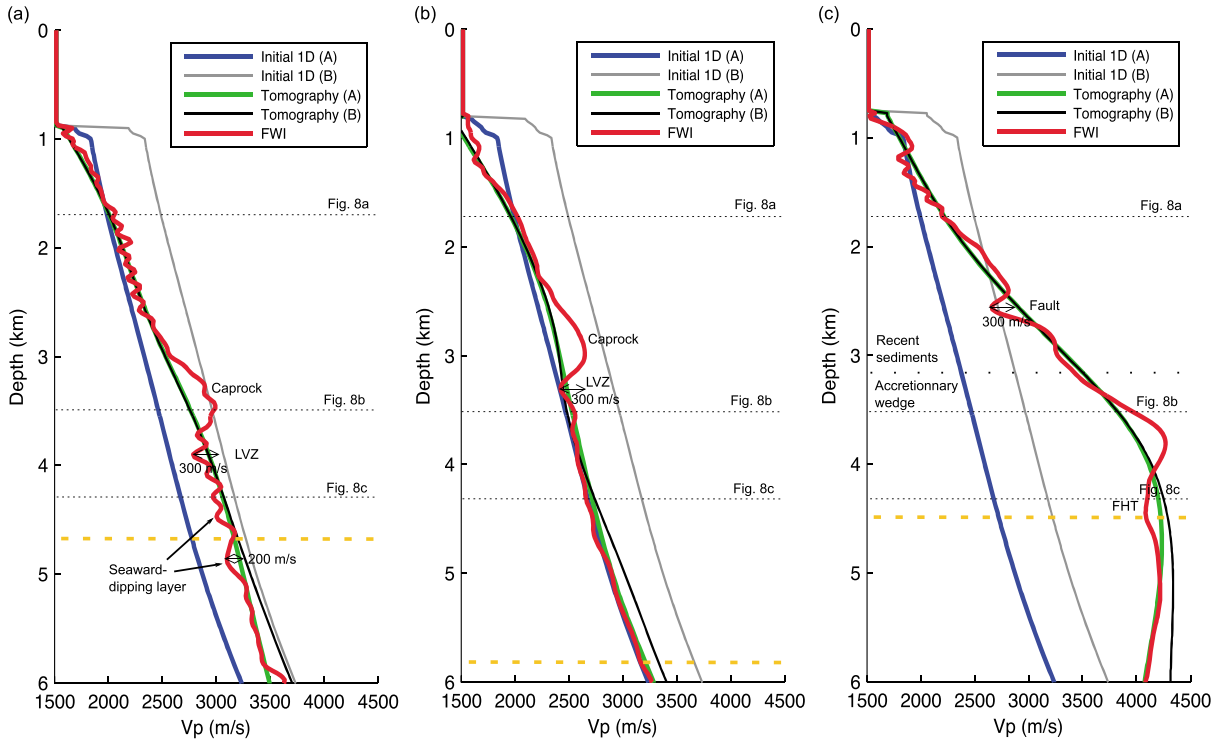

Figure 7. Vertical V_p variations for TTT and FWI V_p models A and B. (a) At 60 km distance. (b) At 39 km distance. (c) At 28 km distance. The dashed orange lines indicate the maximum illumination depth. Main features and corresponding velocity variations are annotated. Narrow black dotted lines indicate the locations of horizontal 1-D plots. Wide black dotted lines indicate the limit between the accretionary wedge sediments and recent sediments.

in the recent sediments, with velocities of about 2.0 km/s increasing to 2.4 km/s in the direction of the forearc high. The velocity then increases abruptly to 3.7 km/s in the accretionary wedge sediments. At 3.5 km depth (Figure 8b), the velocity decreases from 4.2 km/s in the accretionary wedge sediments to 2.4 km/s within the wide LVZ. The 400 m/s drop observed at 23 km distance corresponds to the interpreted forearc high thrust fault. In the thick sediment area, the velocity is around 2.9 km/s. The lower velocity beyond 60 km distance corresponds to a thin LVZ. At 4.25 km depth (Figure 8c), the velocity drops from 4.1 km/s to 2.6 km/s from the accretionary wedge sediments to the LVZ. The highest velocity in the accretionary wedge sediments at this depth is lower than the velocity at 3.5 km depth, because there is no ray coverage at the edge of the model due to the high velocity gradient. In the thick recent sediments, the velocity is about 3.1 km/s. The variations correspond to variations in folded sediments and to a seaward dipping layer at 64 km distance.

6. Porosity Estimation

6.1. Effective Medium Theory

To estimate the porosity and fluid content in the forearc basin, we used EMT, as there is no borehole data in the study area.

EMT relates cracks and pore properties to seismic properties of a given rock by a combination of two methods: a self-consistent approximation (SCA) and differential medium theory (DMT). SCA (Budiansky, 1965; Hill, 1965; Te Wu, 1966) and DMT (Nishizawa, 1982) provide the effective elastic moduli of a medium composed of two different phases by first computing the interaction of the background matrix with a single inclusion of the second phase, and then approximating the interaction of increasing inclusion by replacing the background matrix. The interpretation of the microstructure of SCA is that inclusions will be only interconnected at 40–60% porosity. However, porosity should decrease with depth in the sedimentary section due to compaction. By using the second method, DMT, starting at the value obtained with SCA (Sheng, 1990) in the 40–60% porosity range, we can maintain the interconnectivity of the inclusions below 40%.

The velocity of the material also depends on the geometry of the cracks in the material. EMT defines the geometry of the cracks or inclusions by the aspect ratio depending on the polar and equatorial radius of the

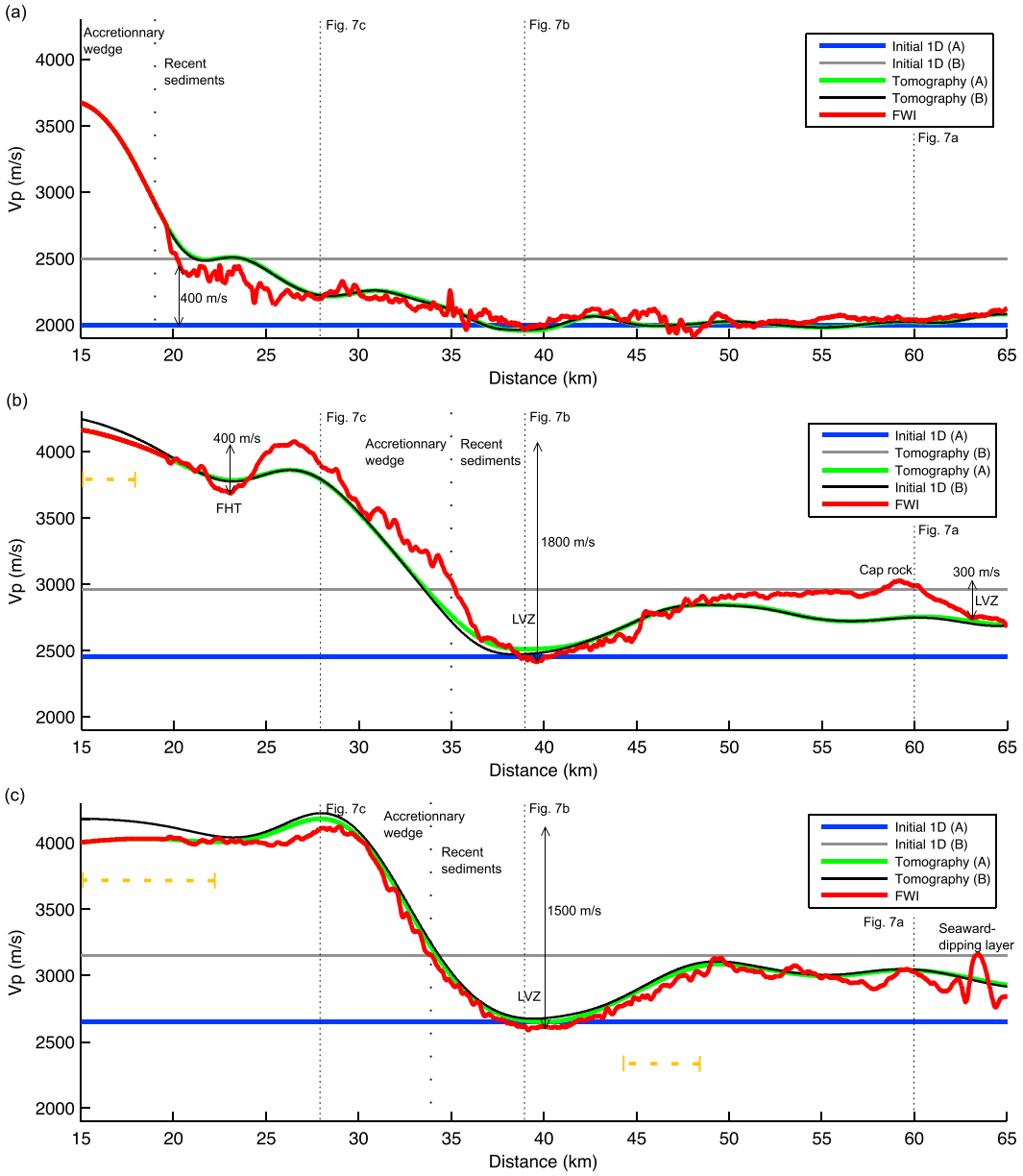

Figure 8. Horizontal V_p variations for TTT and FWI V_p models A and B. (a) At 1.75 km depth. (b) At 3.5 km depth. (c) At 4.25 km depth. The dashed orange lines indicate the part of the line below the maximum illumination depth. Main features and corresponding velocity variations are annotated. Narrow spaced black dotted lines indicate the locations of vertical 1-D plots. Wide-spaced black dotted line indicates the limit between the accretionary wedge sediments and recent sediments.

inclusion. Spherical or randomly oriented ellipsoidal inclusions lead to an isotropic material, whereas aligned ellipsoidal inclusions produce an anisotropic material. In the case of the forearc basin, we can distinguish two geometries. The northeastern part of the profile is composed of horizontally stratified sediments, indicating that the minerals should be horizontally aligned due to compaction. In the southwestern part where the sediments are incoherent and compacted, sediment minerals should be randomly oriented.

6.2. Results of EMT

To discuss the presence of fluid or gas in the sediments at 4 km depth, we correlated the high-definition velocity given by the elastic FWI with the EMT computed for both fluid and gas. We assumed a two-phase EMT composed of a background matrix of sediments with either methane or sea water.

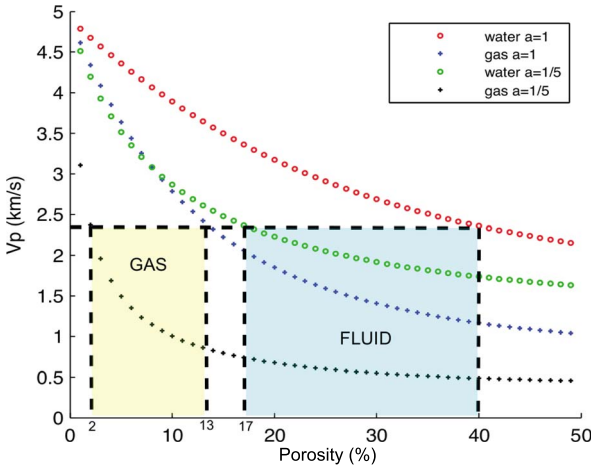

Figure 9. *P* wave velocity as a function of porosity, where pores are either filled with fluid or gas, using effective medium theory for aspect ratios of 1:1 and 1:5. Yellow and blue rectangles indicate the possible gas and fluid ranges, respectively.

As we have no quantitative information about sediment composition in this area, we took as input for the SCA the elastic constant computed from the highest velocity present in the final FWI V_p model located in the accretionary wedge in the western part of the profile. V_s and ρ were linked to V_p by an empirical relationship (Castagna et al., 1985; Gardner et al., 1974). Although the nature of the sediments might change between the accretionary wedge and recent sediments in the forearc basin, both are formed of marine and continental sediments (Mukti et al., 2012). Therefore, we assume that the highest velocity present in the FWI V_p model, 4.9 km/s, corresponds to a pure sedimentary rock with zero porosity. Then we compute elastic constants with the SCA for both fluid and gas to a porosity of 50%. The result is taken as input for the DEM, with which we decreased the porosity back to zero without losing the connectivity of the fluid/gas phase. The gas parameters, which we assume to be methane, were extracted from Batzle and Wang (1992), whereas the fluid phase is sea water.

Figure 9 shows the results of EMT for aspect ratios of 1 (spherical) and 1:5 (ellipsoidal), respectively, which we interpret as incoherent sediment in the west and thick sediment in the east. In order to decrease the velocity to 2.4 km/s in the LVZ, either a maximum of 13% gas or 40% fluid saturation is required, assuming spheroidal inclusions. Assuming ellipsoidal inclusions with an aspect ratio of 1:5, either 2% gas or 17% fluids would be required to reduce the observed *P* wave velocity. By comparison, 1% of gas or 10% of fluid is required to decrease the velocity to 2.9 km/s at the same depth in the thick sediments. We believe that an accumulation of 40% fluid or 13% gas at 4 km depth in a highly deformed region of compacted sediments is unlikely, since such a high quantity of fluid and gas at high pressure would likely be released at the seafloor. The region of the LVZ might be deformed sediments from the northeastern basin, altered sediments from the accretionary wedge, or a mix of both. We assume that the quantity of fluids or gas lies between both end-members, depending of the origin and deformation of the sediments in the LVZ.

Since the porosity computation depends on V_p, an analysis of possible errors due to the uncertainty on V_p is relevant. Checkerboard tests show that there can be a difference up to 200 m/s with the tomography (Figure S3), and below 100 m/s after the FWI (Figure S6) in illuminated areas. This would lead to about 1% difference in the porosity computation for fluid and far below 1% for gas. Therefore, we can assume that the porosity computation is robust and mainly depends on initial assumptions.

7. BSR

The presence of methane has been widely identified through the observation of BSRs in the Andaman Sea and Mentawai forearc basin (Singh et al., 2011; Shankar & Riedel, 2013), methane cold seeps (Siegert et al., 2011) and mud volcanos (Mukti et al., 2012; Samuel & Harbury, 1996). The potential for hydrocarbon generation in biogenic sediments of late Miocene-Pliocene has been suggested by borehole data (Cawthern et al., 2014; Hall et al., 1993; Shankar & Riedel, 2013).

Along the CGGV20 seismic line, Singh et al. (2011) identified a BSR in the anticline to the east of a push-up ridge. BSRs are the seismic signatures of gas hydrates above and a few percent of methane gas below (Singh et al., 1993). A BSR can be identified in seismic data as a strong reflection that usually crosscuts sedimentary reflections and is locally subparallel to the seafloor.

On Figure 10a, a BSR can be seen on both sides of the push-up ridge between 1.6 and 2.0 s TWT above the recent sediments (44 to 48 km distance) and above the compacted sediment (37 to 41 km). The BSR has high amplitudes and crosses the landward dipping folded sediments. Figure 10b shows the V_p final FWI model in the same area. A LVZ can be observed on both sides of the push-up ridge associated with the BSRs in the seismic image. The LVZ on the west side of the push up ridge is at 1.2 km depth, while the one on the east side of the ridge is at 1.4 km depth. Since the seafloor depth is deep enough, the temperature at the sea bottom should not vary significantly (Kvenvolden & Lorenson, 2001; Ruppel, 2007). The difference in depth corresponds to the difference in seafloor bathymetry (~200 m), corresponding to the hydrate stability depth in this region (Rose et al., 2014).

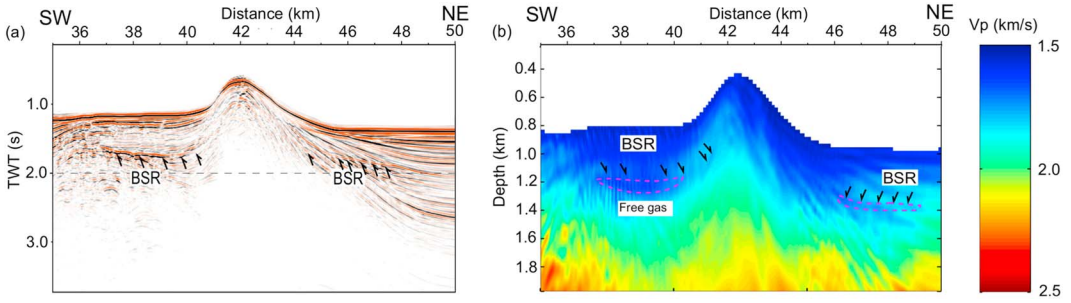

Figure 10. Blow up around the bottom simulating reflectors (BSRs). Light blue lines indicate the location of the BSRs. (a) BSRs on the seismic image. (b) BSRs on the *Vp* model. The purple dashed lines indicate the possible free gas zone.

8. Interpretation of the Results

Figure 11 shows a combined image consisting of the high-resolution FWI velocity model superimposed on the prestack depth migrated seismic image. To correlate properly the FWI velocity results with the seismic imaging, the prestack depth migrated has been conducted using Kirchhoff type migration with the velocity model obtained TTT. Please note that the FWI velocity model was not used for the migration because sharp velocity variations cannot be handled by the ray tracing used in Kirchhoff migration. The TTT velocity model is reliable enough to accurately place the forearc basin features.

The forearc high is characterized by a veneer of recent sediments and associated low velocity, over a high velocity (up to 4.9 km/s) nonreflective sediments, suggesting that these recent sediments are underlain by highly compacted accretionary wedge sediments. The southwestern portion of the forearc basin, between 20 and 35 km distance, contains 1.5–2 km of northeastward dipping sediments, also associated with low velocities and is underlain by high-velocity nonreflective compacted sediments. Further northeast, between 35 km and 42.5 km distance range, up to the push-up ridge, the 2 km thick sediments dip southwestward, and have low velocity as expected. Below this layer, there is a 600 m thick high-velocity layer (HVL), which extends all the way northeast of the profile. The HVL has neither a sharp boundary nor is it associated with any particular seismic reflection. Below this HVL, and beneath the push-up ridge from 35 to 45 km, a large LVZ is present down to 6 km depth. Southwest of the push-up ridge, the transparent reflectivity resembles that of the high-velocity compacted sediments observed in the southwest at similar depths. On the northeast side of the push-up ridge between 42.5 and 50 km, the sediments dip northeastward, with the dip increasing with depth. Then they become nearly flat between 50 and 55 km and start dipping southwestward farther

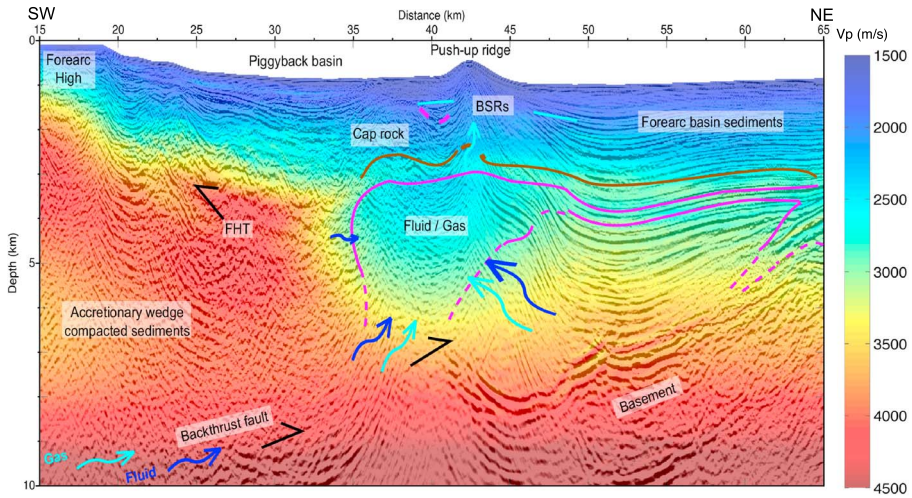

Figure 11. Final FWI V_p model superimposed on the prestack depth migrated seismic image and interpretations. The cap rock is indicated by the brown line. Light blue lines correspond to bottom-simulating reflectors (BSRs) location. Gas and fluid flux are indicated by light and dark blue arrows, respectively. The size of the arrows suggests higher (longer arrows) or lower (smaller arrows) flux. The purple lines indicate possible fluid/gas boundaries.

to the northeast, leading to a maximum sediment thickness of ~6 km between 50 and 55 km. In the vicinity of the push-up ridge and below these layered sediments, the seismic reflectivity is transparent down to the basement at 8 km depth. Since we can image the basement clearly, this lack of reflectivity is real, not an artifact of imaging. In this case, this nonreflective zone might be the continuation of highly compacted accretionary wedge sediments, represented by high velocities. However, the FWI results indicate the presence of a low velocity in this zone, suggesting the presence of fluid/gas. Since the penetration depth of the FWI is down to 6 km, we do not have any constraint on velocity below this depth.

The seismic imaging and porosity estimation suggest that the LVZ corresponds to altered sediments from the accretionary wedge and/or highly deformed forearc basin sediments filled with fluid and gas. The quantity of gas and fluid is difficult to assess with our current data. A small amount of free gas or dissolved gas along with fluids, capped by the 600 m thick HVL observed along the whole profile, is possible in the range of 17–40% of fluid and 2–13% of gas. If we consider that the LVZ sediments are more closely related to forearc basin sediments, the amount of fluid and gas would be closer to the 17% and 2% range limit, respectively. This structure likely corresponds to a mud diapir, as suggested by Mukti et al. (2012).

The formation of mud diapirs or mud volcanoes is driven by buoyancy and abnormal fluid pressure induced by the following conditions (Dimitrov, 2002): tectonic activity more particularly compressional, rapid sedimentation, that is, above 1 mm/yr (Behrmann et al., 2006; Fertl, 1976; Hubbert & Rubey, 1959), a source of carbon, and deeply buried plastic and fine sediments. Tectonic activity in the Mentawai forearc basin has been indeed shown to be compressive by the backthrust imaging (Mukti et al., 2012; Singh et al., 2010). The correlation of field study on land (Samuel et al., 1997) with seismic profiles and well data (Hall et al., 1993) provided composition of the sediments, which include fine-grained mudstones in the deep parts of the basin deposited about 23 My ago (Mukti et al., 2012). The sediments thickness of 6 km (Figure 11) and the 23 My deposit time give an average rate of 0.3 mm/yr. This value is not considered as a rapid sediment deposition rate, and no deposit in the basin exceed 1 mm/yr even in a short time period. However, mud diapirs and mud volcanoes form seaward of the trench in Barbados without compression and with a lower deposit rate (Sumner & Westbrook, 2001). Compressive activity in a thick forearc basin is likely to actively generate mud diapirism or mud volcanism. Moreover, gas would enhanced buoyancy (Brown, 1990).

9. Discussion

The origin of the fluid could either be from local sources, including accretionary wedge sediments and forearc basin sediments, or from deep sources (Brown & Westbrook, 1988; Kopf et al., 2001). Deep sources could include dewatering of underthrust sediments along the plate interface, dewatering of underplated sediments, water released by mineral dehydration,and metamorphism (Kopf et al., 2001). We also suggest that fluid could originate from the mantle wedge alteration through serpentinization (Singh et al., 2011).

As a local fluid source, the accretionary wedge sediments at the SW end of the profile have a very high velocity (4.9 km/s), suggesting that these sediments have been compacted and have little or no fluid. In fact most of the dewatering of the accretionary wedge occurs closer to the trench through compression of accreted sediments and formation of seaward verging thrust faults (Kufner et al., 2014). The Sumatran subduction zone has a wide accretionary wedge; hence, sediments close to the backstop have deformed and dewatered over a long period of time (Le Pichon et al., 1990). Accretionary wedge sediments in the forearc region likely contain no water or only a negligible amount for the LVZ generation.

Contrary to accretionary wedge sediments, the sediments of the forearc basin are likely to be a significant source of fluids. Release of water and mud through mud volcanism has been observed in accretionary complexes such as Barbados (Brown & Westbrook, 1988), Nankai (Toki et al., 2004), and Mediterranean Ridge (Kopf et al., 2001). Overpressured fluids can be released at the surface after fracturing sedimentary layers, forming a mud volcano, or being trapped as a mud diapir due to the presence of a impermeable rock layer or lack of pressure to fracture rocks. Impermeable clays might have been mobilized in a first step by overpressure from rapid loading of the sediments (Barber, 2013), generating a cap rock. Fluids, which could include H_2O and CH_4 rich mud, would then accumulate under the cap rock.

The presence of BSRs along the push-up ridge indicates the presence of methane below. Mud volcanoes/diapirs and BSRs often coexist, due to the mobilization of organic matter from fluid rich sediments. Mentawai forearc deep sediments, interpreted to be late Oligocene-early Miocene, are potential sources of

hydrocarbons (Hall et al., 1993; Mukti et al., 2012). Biotic hydrocarbons could form in the deepest part of the basin and migrate in the reservoir rocks forming the LVZ. Gas expelled by mud volcanoes is generally dissolved; however, free gas bubble could be present, most likely in shallow areas (Deville et al., 2006). As the solubility of gas in water is limited (although increased with depth) and is decreased in saline water (Brown, 1990), free gas bubble could be present at depth in presence of a high quantity of gas, particularly in a trapped environment such as a mud diapir.

Fluids could also have a deep origin, flowing along the plate interface to the forearc basin through the backthrust fault. Underthrust and underplated sediments mainly release fluids by mineral dehydration and metamorphic reactions at depth. Most of the water is released near the backstop (Kopf et al., 2001; Kufner et al., 2014). Fluids of deep origin have been observed to flow along the backthrust and form mud volcanoes in Nankai (Kopf, 2013) and Barbados (Brown & Westbrook, 1988). Kufner et al. (2014) show by modeling the Mediterranean Ridge that pore pressure remain high at the décollement along the slab toward the backstop. Pore pressure decreases near the backstop as fluids are released in the forearc (Kufner et al., 2014), resulting in an increase of shear stress that could mark the up-dip limit of the seismogenic zone (Scholz, 1998). Presence of mud diapirs and mud volcanos have been attributed to high pore fluid pressure below the accretionary wedge (Brown & Westbrook, 1988; von Huene & Lee, 1982). However, the subduction front in this region has unexpectedly ruptured up to the toe of the accretionary wedge in 2010 (Lay et al., 2011), independently from the rupture of the forearc region that occurred in 2007. A low pore fluid pressure at the décollement along the plate interface could be interpreted from the occurrence of these events, though recent studies show that earthquakes can occur in regions where overpressured fluids were inferred (e.g., Saffer & Wallace, 2015). However, mélange, interpreted as ancient mud diapirs or volcanoes, is present on Siberut, Nias Islands, and other Sumatran forearc islands (Samuel & Harbury, 1996). The origin of the mélange has been identified as subduction interface fluids (Barber, 2013; Samuel & Harbury, 1996). Formation of mud diapirs and mud volcanoes is still active in Sumatran forearc islands (Barber, 2013), suggesting an efficient drainage of fluid before the backstop, hence a lower amount of fluids released in the forearc basin from underthrust and underplated sediments.

Based on strong reflectivity of the backthrusts in the 2004 and 2007 earthquake rupture zones and weak reflectivity in the locked and aseismic zones, Singh et al. (2011) suggested that this enhanced reflectivity of the backthrust in the 2004 and 2007 earthquake rupture zones could be due to the presence of fluids from the mantle wedge expelled after these great earthquakes along the reactivated backthrusts. Overpressured fluids within the serpentinized mantle wedge would be easily mobilized in the form of serpentine mud. The presence of a low-velocity anomaly beneath the forearc at 30 km depth has been interpreted as serpentinization of the toe of the mantle wedge (Collings et al., 2012). The release of fluids carried by sediments along the plate interface would serpentinize the mantle wedge, which can be easily eroded as compared to gabbroic continental rocks, particularly by topography on the downgoing plate (Singh et al., 2011). Thermal modeling demonstrated that the temperature of the slab surface at 30 km depth (>200°C) in Central Sumatra would be sufficient for water release through dehydration (Syracuse et al., 2010; van Keken et al., 2011). The presence of the 2 km thick piggyback basin southwest of the push-up ridge and up to 6 km of sediments in the northeast suggests that there are two active processes in this region: thrusting along the southwest dipping backthrust forming the push-up ridge and piggyback basin (Mukti et al., 2012), and subsidence forming the southwestward tilting sedimentary basin. Basal erosion of the forearc mantle wedge has been proposed to explain the subsidence in the Andaman forearc, North Sumatra (Cochran, 2010; Moeremans & Singh, 2015). Forearc study from Alaska suggests that subsidence is likely to be linked with asperities at plate interface (Wells et al., 2003). The subsidence could also be caused by the change in the locking mechanisms (from locked in the southwest to aseismic slip in the northeast) at the plate interface (e.g., Hyndman, 2013; Kelson et al., 2012) or due to the erosion of the mantle wedge. The downdip limit of the 2007 earthquake at 45 km depth suggests that the locking depth should extend further northeast from the forearc basin, close to the Sumatran continental margin.

The presence of deep rooted fluids in the form of serpentine mud diapirs have been reported in several subduction systems (i.e., the Marianas forearc region, the Barbados accretionary wedge, the Mediterranean accretionary wedge, Brown & Westbrook, 1988; Fryer et al., 1990; Kopf, 2002; Kopf et al., 2001; Maekawa et al., 2003). In the Marianas arc region, mud volcanoes have been observed between 45 and 90 km from the trench axis, containing traces of serpentinite clasts of mantle wedge origin and are associated with deep-rooted faults (Hulme et al., 2010). Mélange that contain clasts of blueschists, eclogites in a serpentinous matrix has been

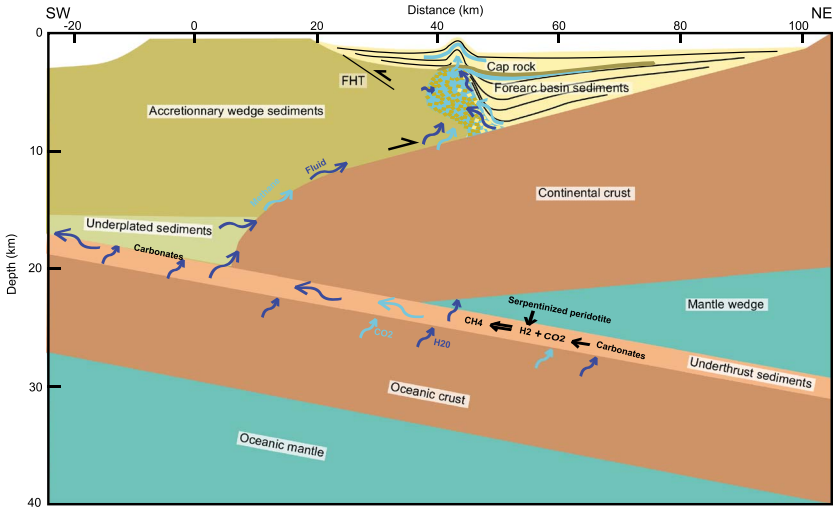

Figure 12. Schematic representation of fluid and gas origin, and flux to the forearc basin. Arrows indicate fluid (dark blue) and gas (light blue) flux. Continental and oceanic crusts are colored in brown, continental mantle and oceanic mantle are colored in green. Accretionary wedge sediments are in dark yellow, forearc recent sediments are in light yellow.

suggested to originate from the mantle (Cloos, 1984). However, no clast of blueschist or eclogite have been recorded from the mélange on the forearc Sunda Islands. The possible low shear stress at the plate interface and the presence of mélange from below the accretionary wedge in forearc island could indicate an efficient drainage of fluids before the forearc. Fluids from deeper origin would rather flow only along the backthrust rather than in deep-rooted faults below the accretionary wedge.

Elastic FWI has also been applied on line CGGV10 in the forearc basin in the locked zone north of the 2007 rupture zone (Wang et al., 2014). Results only show the presence of a narrow LVZ, and the whitened zone beneath the push-up ridge indicates the presence of gas (Wang et al., 2014). The seismic line CGGV20, which has high reflectivity, is bounded by CGGV10 and CGGV40 seismic lines, showing poor reflectivity only 100 km away, in the locked and aseismic zone, respectively (Singh et al., 2011). The occurrence of the 2010 shallow rupture in this region (low pore fluid pressure at the plate interface and high drainage before the forearc) and high reflectivity of the backthrust might indicate that fluids have a mantle origin rather than coming from underthrust and underplated sediments (Figure 12). Earthquakes might increase pore fluid pressure at the serpentinized mantle wedge and facilitate fluid flow, explaining the difference of reflectivity in ruptured and nonruptured area (Singh et al., 2011). Abiotic methane could be generated by a reaction between H_2 from serpentinization and CO or CO_2 from thermal metamorphism of carbonates (Giardini & Salotti, 1969). In addition, hydrocarbons could be generated in the deeper part of the subduction zone under mantle conditions (Scott et al., 2004; Sharma et al., 2009). Ague and Nicolescu (2014) demonstrated the implication of metacarbonate dissolution along the slab based on CO_2 release in the volcanic arc in Greece by studying carbonate dissolution in a forearc setting. Manning (2014) also suggested the release of CO_2 and CH_4 in the forearc basin.

Although fluid and gas rising from the serpentinized mantle wedge is not excluded in the Mentawai forearc basin, chemical analysis of carbon and hydrogen isotopes from methane seep or from borehole samples from the large LVZ would be required (Etiope & Schoell, 2014; Sephton & Hazen, 2013; Siegert et al., 2011). Such data would make it possible to quantify proportion of fluid and gas from the forearc basin sediments, and identify their origin, either from underthrust and underplated sediments or from the serpentinized mantle wedge.

10. Conclusion

The forearc basin in the 2007 rupture zone is characterized by thick recent sediments in the northeast over the continental basement, a thin piggyback basin in the southwest above eroded accretionary wedge sediments or highly deformed forearc basin sediments, and a push-up ridge dividing the two zones. A backthrust beneath the piggyback basin, which also forms a continental backstop, might be responsible for the formation of the push-up ridge, and might be a conduit for fluid release in the forearc basin. FWI of 15 km long offset

streamer data provides a detailed velocity structure of the basin, which combined with the prestack depth migration allows us to identify the following important features:

1. The presence of a BSR ~400 m below the seafloor associated with a low velocity underneath, possibly associated with methane gas.
2. A 600 m thick HVL is present along a significant part of the profile, forming a cap rock for the low-velocity layer underneath. This layer might correspond to clays mobilized by loading and overpressure.
3. A 4 km thick and 10 km long low-velocity anomaly beneath the push-up ridge and above the backthrust, which we interpret to be a mud diapir. Current data do not enable to conclude on the origin of the fluid and gas. The highest contribution should originate from forearc basin sediments, but a nonnegligible part might also rise from the plate interface or the serpentinized mantle wedge.

Acknowledgments
This project was funded by GPX partners and the French ANR under the grant ANR-12-CHIN-0003. The seismic data were provided by CGG. This work was granted access to the HPC resources of IDRIS under the allocation 2014-100334 made by GENCI. We thank D. Shillington, J. Hubbard, the first and third anonymous reviewers for their thorough analysis, comments, and suggestions on the interpretation of this work. We also thank S. Operto, M. Noble, and the second anonymous reviewer for their comments and suggestions on the technical aspect of this work. The data for this paper are available by contacting Huot G. at huot@ipgp.fr. This is IPGP contribution number 3924.

References

Ague, J. J., & Nicolescu, S. (2014). Carbon dioxide released from subduction zones by fluid-mediated reactions. *Nature Geoscience*, *7*(5), 355–360. https://doi.org/10.1038/ngeo2143

Amin, T. C., Kusnama, E. R., & Gafoer, S. (1993). Geological map of the Manna and Enggano sheet, Sumatra, scale 1:250.000. In *Geological Research and Development Center*. Bandung, Indonesia.

Andi Mangga, S., Burhan Sukardi, G., & Suryanila, E. (1994). Geological map of the Siberut sheet, Sumatra, scale 1:250.000. In *Geological Research and Development Center*. Bandung, Indonesia.

Arnulf, A., Harding, A., Kent, G., Singh, S., & Crawford, W. (2014). Constraints on the shallow velocity structure of the Lucky Strike volcano, mid-Atlantic ridge, from downward continued multichannel streamer data. *Journal of Geophysical Research: Solid Earth*, *119*, 1119–1144. https://doi.org/10.1002/2013JB010500

Arnulf, A., Harding, A., Singh, S., Kent, G., & Crawford, W. (2012). Fine-scale velocity structure of upper oceanic crust from full waveform inversion of downward continued seismic reflection data at the Lucky Strike volcano, mid-Atlantic ridge. *Geophysical Research Letters*, *39*, L08303. https://doi.org/10.1029/2012GL051064

Barber, A. (2013). The origin of mélanges: Cautionary tales from Indonesia. *Journal of Asian Earth Sciences*, *76*, 428–438. https://doi.org/10.1016/j.jseaes.2012.12.021

Barnes, C., & Charara, M. (2009). The domain of applicability of acoustic full-waveform inversion for marine seismic data. *Geophysics*, *74*(6), WCC91–WCC103. https://doi.org/10.1190/1.3250269

Batzle, M., & Wang, Z. (1992). Seismic properties of pore fluids. *Geophysics*, *57*(11), 1396–1408. https://doi.org/10.1190/1.1443207

Behrmann, J. H., Flemings, P. B., & John, C. M. (2006). Rapid sedimentation, overpressure, and focused fluid flow, Gulf of Mexico continental margin. *Scientific Drilling*, *3*, 12–17. https://doi.org/10.2204/iodp.sd.3.03.2006

Bellier, O., Bellon, H., Sébrier, M., & Maury, R. C. (1999). K-Ar age of the Ranau tuffs: Implications for the Ranau caldera emplacement and slip-partitioning in Sumatra (Indonesia). *Tectonophysics*, *312*(2), 347–359. https://doi.org/10.1016/S0040-1951(99)00198-5

Briggs, R. W., Sieh, K., Meltzner, A. J., Natawidjaja, D., Galetzka, J., Suwargadi, B., … Suprihanto, I. (2006). Deformation and slip along the Sunda megathrust in the great 2005 Nias-Simeulue earthquake. *Science*, *311*(5769), 1897–1901. https://doi.org/10.1126/science.1122602

Brown, K. M. (1990). The nature and hydrogeologic significance of mud diapirs and diatremes for accretionary systems. *Journal of Geophysical Research*, *95*(B6), 8969–8982. https://doi.org/10.1029/JB095iB06p08969

Brown, K., & Westbrook, G. K. (1988). Mud diapirism and subcretion in the Barbados Ridge Accretionary Complex: The role of fluids in accretionary processes. *Tectonics*, *7*(3), 613–640. https://doi.org/10.1029/TC007i003p00613

Budhitrisna, T., & Andi Mangga, S. (1990). Geological map of the Pagai and Sipora quadrangle, Sumatra, scale 1:250.000. In *Geological Research and Development Center*. Bandung, Indonesia.

Budiansky, B. (1965). On the elastic moduli of some heterogeneous materials. *Journal of the Mechanics and Physics of Solids*, *13*(4), 223–227. https://doi.org/10.1016/0022-5096(65)90011-6

Bunks, C., Saleck, F. M., Zaleski, S., & Chavent, G. (1995). Multiscale seismic waveform inversion. *Geophysics*, *60*(5), 1457–1473. https://doi.org/10.1190/1.1443880

Castagna, J. P., Batzle, M. L., & Eastwood, R. L. (1985). Relationships between compressional-wave and shear-wave velocities in clastic silicate rocks. *Geophysics*, *50*(4), 571–581. https://doi.org/10.1190/1.1441933

Cawthern, T., Johnson, J., Giosan, L., Flores, J., Rose, K., & Solomon, E. (2014). A late Miocene-Early Pliocene biogenic silica crash in the Andaman Sea and Bay of Bengal. *Marine and Petroleum Geology*, *58*, 490–501. https://doi.org/10.1016/j.marpetgeo.2014.07.026

Chauhan, A. P., Singh, S. C., Hananto, N. D., Carton, H., Klingelhoefer, F., Dessa, J.-X., … Team, S. S. (2009). Seismic imaging of forearc backthrusts at northern Sumatra subduction zone. *Geophysical Journal International*, *179*(3), 1772–1780. https://doi.org/10.1111/j.1365-246X.2009.04378.x

Cloos, M. (1984). Flow melanges and the structural evolution of accretionary wedges. *Geological Society of America Special Papers*, *198*, 71–80. https://doi.org/10.1130/SPE198-p71

Cochran, J. R. (2010). Morphology and tectonics of the Andaman forearc, northeastern Indian Ocean. *Geophysical Journal International*, *182*(2), 631–651. https://doi.org/10.1111/j.1365-246X. 2010.04663.x

Collings, R., Lange, D., Rietbrock, A., Tilmann, F., Natawidjaja, D., Suwargadi, B., … Saul, J. (2012). Structure and seismogenic properties of the Mentawai segment of the Sumatra subduction zone revealed by local earthquake traveltime tomography. *Journal of Geophysical Research*, *117*, B01312. https://doi.org/10.1029/2011JB008469

Crase, E., Pica, A., Noble, M., McDonald, J., & Tarantola, A. (1990). Robust elastic nonlinear waveform inversion: Application to real data. *Geophysics*, *55*(5), 527–538. https://doi.org/10.1190/1.1442864

Deville, E., Guerlais, S.-H., Callec, Y., Griboulard, R., Huyghe, P., Lallemant, S., … the Collaboration of the Caramba working Group (2006). Liquefied vs stratified sediment mobilization processes: Insight from the South of the Barbados accretionary prism. *Tectonophysics*, *428*(1), 33–47. https://doi.org/10.1016/j.tecto.2006.08.011

Diament, M., Harjono, H., Karta, K., Deplus, C., Dahrin, D., Zen, M., … Malod, J. (1992). Mentawai fault zone off Sumatra: A new key to the geodynamics of western Indonesia. *Geology*, *20*(3), 259–262. https://doi.org/10.1130/0091-7613(1992)020<0259:MFZOSA>2.3.CO;2

Dimitrov, L. I. (2002). Mud volcanoes—The most important pathway for degassing deeply buried sediments. *Earth-Science Reviews*, *59*(1), 49–76. https://doi.org/10.1016/S0012-8252(02)00069-7

Etiope, G., & Schoell, M. (2014). Abiotic gas: Atypical, but not rare. *Elements*, *10*(4), 291–296. https://doi.org/10.2113/gselements.10.4.291
Fertl, W. (1976). Abnormal formation pressures: Implications to exploration. In *Drilling, and Production of Oil and Gas Resources*. Amsterdam: Elsevier.
Fitch, T. J. (1972). Plate convergence, transcurrent faults, and internal deformation adjacent to southeast Asia and the western Pacific. *Journal of Geophysical Research*, *77*(23), 4432–4460. https://doi.org/10.1029/JB077i023p04432
Fountain, D. M., Hurich, S. B., & Smithson, C. A. (1984). Seismic reflectivity of mylonite zones in the crust. *Geology*, *12*(4), 195. https://doi.org/10.1130/0091-7613(1984)12<195:SROMZI>2.0.CO;2
Fryer, P., Saboda, K. L., Johnson, L. E., Mackay, M. E., Moore, G. F., & Stoffers, P. (1990). Conical seamount: SeaMARC II, Alvin submersible, and seismic reflection studies. In *Proceedings of the Ocean Drilling Program: Initial Reports, Leg 125, College Station, Texas, Ocean Drilling Program* (pp. 5–14). https://doi.org/10.2973/odp.proc.ir.125.104.1990
Gardner, G., Gardner, L., & Gregory, A. (1974). Formation velocity and density—The diagnostic basics for stratigraphic traps. *Geophysics*, *39*(6), 770–780. https://doi.org/10.1190/1.1440465
Ghosal, D., Singh, S., & Martin, J. (2014). Shallow subsurface morphotectonics of the NW Sumatra subduction system using an integrated seismic imaging technique. *Geophysical Journal International*, *198*(3), 1818–1831. https://doi.org/10.1093/gji/ggu182
Giardini, A., & Salotti, C. (1969). Kinetics and relations in the calcite-hydrogen reaction and relations in the dolomite-hydrogen and siderite-hydrogen systems. *American Mineralogist*, *54*, 1151–1172.
Hall, D., Duff, B., Courbe, M., Seubert, B., Siahaan, M., & Wirabudi, A. (1993). The southern fore-arc zone of Sumatra: Cainozoic basin-forming tectonism and hydrocarbon potential. In *Proceedings of the 22nd Annual Convention, Jakarta, Indonesian Petroleum Association* (Vol. 1, pp. 319–344).
Hill, R. (1965). A self-consistent mechanics of composite materials. *Journal of the Mechanics and Physics of Solids*, *13*(4), 213–222. https://doi.org/10.1016/0022-5096(65)90010-4
Hubbert, M. K., & Rubey, W. W. (1959). Role of fluid pressure in mechanics of overthrust faulting: I. Mechanics of fluid-filled porous solids and its application to overthrust faulting. *Geological Society of America Bulletin*, *70*(2), 115–166. https://doi.org/10.1130/0016-7606(1959)70[115:ROFPIM]2.0.CO;2
Hulme, S. M., Wheat, C. G., Fryer, P., & Mottl, M. J. (2010). Pore water chemistry of the Mariana serpentinite mud volcanoes: A window to seismogenic zone. *Geochemistry, Geophysics, Geosystems*, *11*, Q01X09. https://doi.org/10.1029/2009GC002674
Hyndman, R. D. (2013). Downdip landward limit of Cascadia great earthquake rupture. *Journal of Geophysical Research: Solid Earth*, *118*, 5530–5549. https://doi.org/10.1002/jgrb.50390
Jian, H., Li, J., Chen, Y. J., Singh, S. C., Ruan, A., Qiu, X., & Zhao, M. (2012). Three-dimensional seismic tomography reveals the presence of partial melt in the lower crust of the ultraslow Southwest Indian Ridge at 50°28′E. Abstract OS11E-02 Presented at the 2012 AGU Fall Meeting, San Francisco, CA.
Kelson, K., Witter, R. C., Tassara, A., Ryder, I., Ledezma, C., Montalva, G., … Johnson, L. (2012). Coseismic tectonic surface deformation during the 2010 Maule, Chile, M_w 8.8 earthquake. *Earthquake Spectra*, *28*(S1), S39–S54. https://doi.org/10.1193/1.4000042
Konca, A. O., Avouac, J.-P., Sladen, A., Meltzner, A. J., Sieh, K., Fang, P., … Chlieh, M. (2008). Partial rupture of a locked patch of the Sumatra megathrust during the 2007 earthquake sequence. *Nature*, *456*(7222), 631–635. https://doi.org/10.1038/nature07572
Kopf, A. (2013). *Report and preliminary results of RV SONNE cruise SO222 MEMO (MeBo drilling and in situ long-term monitoring in the Nankai Trough Accretionary Complex* (Vol. 297). Japan: Berichte aus dem Fachbereich Geowissenschaften der Universität Bremen.
Kopf, A. J. (2002). Significance of mud volcanism. *Reviews of Geophysics*, *40*(2), 1005. https://doi.org/10.1029/2000RG000093
Kopf, A. J., Klaeschen, D., & Mascle, J. (2001). Extreme efficiency of mud volcanism in dewatering accretionary prisms. *Earth and Planetary Science Letters*, *189*, 295–313. https://doi.org/10.1016/S0012-821X(01) 00278-3
Kopp, H., & Kukowski, N. (2003). Backstop geometry and accretionary mechanics of the Sunda margin. *Tectonics*, *22*(6), 1072. https://doi.org/10.1029/2002TC001420
Kopp, H., Flueh, E. R., Klaeschen, D., Bialas, J., & Reichert, C. (2001). Crustal structure of the central Sunda margin at the onset of oblique subduction. *Geophysical Journal International*, *147*(2), 449–474. https://doi.org/10.1046/j.0956-540X.2001.01547.x
Kufner, S.-K., Hüpers, A., & Kopf, A. (2014). Constraints on fluid flow processes in the Hellenic Accretionary Complex (eastern Mediterranean Sea) from numerical modeling. *Journal of Geophysical Research: Solid Earth*, *119*, 3601–3626. https://doi.org/10.1002/2013JB010405
Kvenvolden, K. A., & Lorenson, T. D. (2001). *The global occurrence of natural gas hydrate*. Washington, DC: Wiley Online Library. https://doi.org/10.1029/GM124p0003
Lailly, P. (1983). The seismic inverse problem as a sequence of before stack migration. In *Conference on Inverse Scattering, Theory and Applications, Philadelphia, Society for Industrial and Applied Mathematics, Expanded Abstracts* (pp. 206–220).
Lay, T., Ammon, C., Kanamori, H., Yamazaki, Y., Cheung, K., & Hutko, A. (2011). The 25 October 2010 Mentawai tsunami earthquake (M_w 7.8) and the tsunami hazard presented by shallow megathrust ruptures. *Geophysical Research Letters*, *38*, L06302. https://doi.org/10.1029/2010GL046552
Le Pichon, X., Henry, P., & Lallemant, S. (1990). Water flow in the Barbados accretionary complex. *Journal of Geophysical Research*, *95*(B6), 8945–8967. https://doi.org/10.1029/JB095iB06p08945
Levander, A. R. (1988). Fourth-order finite-difference P-SV seismograms. *Geophysics*, *53*(11), 1425–1436. https://doi.org/10.1190/1.1442422
Maekawa, H., Shozui, M., Ishii, T., Fryer, P., & Pearce, J. A. (2003). Blueschist metamorphism in an active subduction zone. *Nature*, *364*(6437), 520–523. https://doi.org/10.1038/364520a0
Manning, C. E. (2014). Geochemistry: A piece of the deep carbon puzzle. *Nature Geoscience*, *7*(5), 333–334. https://doi.org/10.1038/ngeo2152
McCaffrey, R., Zwick, P. C., Bock, Y., Prawirodirdjo, L., Genrich, J. F., Stevens, C. W., … Subarya, C. (2000). Strain partitioning during oblique plate convergence in northern Sumatra: Geodetic and seismologic constraints and numerical modeling. *Journal of Geophysical Research*, *105*(B12), 28363–28376. https://doi.org/10.1029/1999JB900362
McNeill, L. C., & Henstock, T. J. (2014). Forearc structure and morphology along the Sumatra-Andaman subduction zone. *Tectonics*, *33*, 112–134. https://doi.org/10.1002/2012TC003264
Milkov, A. (2000). Worldwide distribution of submarine mud volcanoes and associated gas hydrates. *Marine Geology*, *167*(1), 29–42. https://doi.org/10.1016/S0025-3227(00)00022-0
Moeremans, R. E., & Singh, S. C. (2015). Fore-arc basin deformation in the Andaman-Nicobar segment of the Sumatra-Andaman subduction zone: Insight from high-resolution seismic reflection data. *Tectonics*, *34*, 1736–1750. https://doi.org/10.1002/2015TC003901
Mora, P. (1987). Nonlinear two-dimensional elastic inversion of multi-offset seismic data. *Geophysics*, *52*(9), 1211–1228. https://doi.org/10.1190/1.1442384
Moser, T. (1991). Shortest path calculation of seismic rays. *Geophysics*, *56*(1), 59–67. https://doi.org/10.1190/1. 1442958

Mukti, M., Singh, S. C., Deighton, I., Hananto, N. D., Moeremans, R., & Permana, H. (2012). Structural evolution of backthrusting in the Mentawai fault zone, offshore Sumatran forearc. *Geochemistry, Geophysics, Geosystems*, *13*, Q12006. https://doi.org/10.1029/2012GC004199

Muller, R. D., Sdrolias, M., Gaina, C., & Roest, W. R. (2008). Age, spreading rates, and spreading asymmetry of the world's ocean crust. *Geochemistry, Geophysics, Geosystems*, *9*, Q04006. https://doi.org/10.1029/2007GC001743

Natawidjaja, D. H., Sieh, K., Chlieh, M., Galetzka, J., Suwargadi, B. W., Cheng, H., … Ward, S. N. (2006). Source parameters of the great Sumatran megathrust earthquakes of 1797 and 1833 inferred from coral microatolls. *Journal of Geophysical Research*, *111*, B06403. https://doi.org/10.1029/2005JB004025

Newcomb, K., & McCann, W. (1987). Seismic history and seismotectonics of the Sunda arc. *Journal of Geophysical Research*, *92*(B1), 421–439. https://doi.org/10.1029/JB092iB01p00421

Nishizawa, O. (1982). Seismic velocity anisotropy in a medium containing oriented cracks. *Journal of Physics of the Earth*, *30*(4), 331–347. https://doi.org/10.4294/jpe1952.30.331

Pica, A., Diet, J., & Tarantola, A. (1990). Nonlinear inversion of seismic reflection data in a laterally invariant medium. *Geophysics*, *55*(3), 284–292. https://doi.org/10.1190/1.1442836

Plessix, R.-E. (2006). A review of the adjoint-state method for computing the gradient of a functional with geophysical applications. *Geophysical Journal International*, *167*(2), 495–503. https://doi.org/10.1111/j.1365-246X.2006. 02978.x

Prawirodirdjo, L., & Bock, Y. (2004). Instantaneous global plate motion model from 12 years of continuous GPS observations. *Journal of Geophysical Research*, *109*, B08405. https://doi.org/10.1029/2003JB002944

Rose, K. K., Johnson, J. E., Torres, M. E., Hong, W.-L., Giosan, L., Solomon, E. A., … Schaef, H. T. (2014). Anomalous porosity preservation and preferential accumulation of gas hydrate in the Andaman accretionary wedge, NGHP-01 site 17a. *Marine and Petroleum Geology*, *58*, 99–116. https://doi.org/10.1016/j.marpetgeo.2014.04.009

Ruppel, C. (2007). Tapping methane hydrates for unconventional natural gas. *Elements*, *3*(3), 193–199. https://doi.org/10.2113/gselements.3.3.193

Saffer, D. M., & Wallace, L. M. (2015). The frictional, hydrologic, metamorphic and thermal habitat of shallow slow earthquakes. *Nature Geoscience*, *8*(8), 594–600. https://doi.org/10.1038/ngeo2490

Samuel, M., & Harbury, N. (1996). The Mentawai fault zone and deformation of the Sumatran forearc in the Nias area. *Geological Society, London, Special Publications*, *106*(1), 337–351. https://doi.org/10.1144/GSL.SP.1996.106.01.22

Samuel, M., Harbury, N., Bakri, A., Banner, F., & Hartono, L. (1997). A new stratigraphy for the islands of the Sumatran forearc, Indonesia. *Journal of Asian Earth Sciences*, *15*(4), 339–380. https://doi.org/10.1016/S0743-9547(97)87720-3

Schlüter, H., Gaedicke, C., Roeser, H., Schreckenberger, B., Meyer, H., Reichert, C., … Prexl, A. (2002). Tectonic features of the southern Sumatra-western Java forearc of Indonesia. *Tectonics*, *21*(5), 1047. https://doi.org/10.1029/2001TC901048

Scholz, C. H. (1998). Earthquakes and friction laws. *Nature*, *391*(6662), 37. https://doi.org/10.1038/34097

Scott, H. P., Hemley, R. J., Mao, H.-k., Herschbach, D. R., Fried, L. E., Howard, W. M., & Bastea, S. (2004). Generation of methane in the Earth's mantle: In situ high pressure-temperature measurements of carbonate reduction. *Proceedings of the National Academy of Sciences of the United States of America*, *101*(39), 14,023–14,026. https://doi.org/10.1073/pnas.0405930101

Sephton, M. A., & Hazen, R. M. (2013). On the origins of deep hydrocarbons. *Reviews in Mineralogy and Geochemistry*, *75*, 449–465. https://doi.org/10.2138/rmg.2013.75.14

Shankar, U., & Riedel, M. (2013). Heat flow and gas hydrate saturation estimates from Andaman Sea, India. *Marine and Petroleum Geology*, *43*, 434–449. https://doi.org/10.1016/j.marpetgeo.2012.12.004

Sharma, A., Cody, G. D., & Hemley, R. J. (2009). In situ diamond-anvil cell observations of methanogenesis at high pressures and temperatures. *Energy & Fuels*, *23*(11), 5571–5579. https://doi.org/10.1021/ef9006017

Sheng, P. (1990). Effective-medium theory of sedimentary rocks. *Physical Review B*, *41*(7), 4507. https://doi.org/10.1103/PhysRevB.41.4507

Shipp, R. M., & Singh, S. C. (2002). Two-dimensional full wavefield inversion of wide-aperture marine seismic streamer data. *Geophysical Journal International*, *151*(2), 325–344. https://doi.org/10.1046/j.1365-246X.2002.01645.x

Siegert, M., Krüger, M., Teichert, B., Wiedicke, M., & Schippers, A. (2011). Anaerobic oxidation of methane at a marine methane seep in a forearc sediment basin off Sumatra, Indian Ocean. *Frontiers in Microbiology*, *2*, 249. https://doi.org/10.3389/fmicb.2011.00249

Sieh, K., & Natawidjaja, D. (2000). Neotectonics of the Sumatran fault, Indonesia. *Journal of Geophysical Research*, *105*(B12), 28295–28326. https://doi.org/10.1029/2000JB900120

Singh, S., Hananto, N., & Chauhan, A. (2011). Enhanced reflectivity of backthrusts in the recent great Sumatran earthquake rupture zones. *Geophysical Research Letters*, *38*, L04302. https://doi.org/10.1029/2010GL046227

Singh, S. C., Hananto, N. D., Chauhan, A. P., Permana, H., Denolle, M., Hendriyana, A., & Natawidjaja, D. (2010). Evidence of active backthrusting at the NE margin of Mentawai Islands, SW Sumatra. *Geophysical Journal International*, *180*(2), 703–714. https://doi.org/101111/j.1365-246X.2009.04458x

Singh, S. C., Midenet, S., & Djajadihardja, Y. (2009). Seismic survey of the locked and unlocked Sumatra subduction zone. *Eos, Transactions American Geophysical Union*, *90*(49), 471–471. https://doi.org/10.1029/2009EO490002

Singh, S. C., Minshull, T. A., & Spence, G. D. (1993). Velocity structure of a gas hydrate reflector. *Science-New York Then Washington*, *260*, 204–204. https://doi.org/10.1126/science.260.5105.204

Sirgue, L. (2006). The importance of low frequency and large offset in waveform inversion. In *68th EAGE Conference and Exhibition Incorporating SPE EUROPEC 2006*. London, UK. https://doi.org/10.3997/2214-4609.201402146

Sumner, R. H., & Westbrook, G. K. (2001). Mud diapirism in front of the Barbados accretionary wedge: the influence of fracture zones and North America-South America plate motions. *Marine and Petroleum Geology*, *18*(5), 591–613. https://doi.org/10.1016/S0264-8172(01)00010-1

Syracuse, E. M., van Keken, P. E., & Abers, G. A. (2010). The global range of subduction zone thermal models. *Physics of the Earth and Planetary Interiors*, *183*(1), 73–90. https://doi.org/10.1016/j.pepi.2010.02.004

Tarantola, A. (1984). Inversion of seismic reflection data in the acoustic approximation. *Geophysics*, *49*(8), 1259–1266. https://doi.org/10.1190/1.1441754

Te Wu, T. (1966). The effect of inclusion shape on the elastic moduli of a two-phase material. *International Journal of Solids and Structures*, *2*(1), 1–8. https://doi.org/10.1016/0020-7683(66)90002-3

Toki, T., Tsunogai, U., Gamo, T., Kuramoto, S., & Ashi, J. (2004). Detection of low-chloride fluids beneath a cold seep field on the Nankai accretionary wedge off Kumano, south of Japan. *Earth and Planetary Science Letters*, *228*(1), 37–47. https://doi.org/10.1016/j.epsl.2004.09.007

Van Avendonk, H. J., Harding, A. J., Orcutt, J. A., & McClain, J. S. (1998). A two-dimensional tomographic study of the Clipperton transform fault. *Journal of Geophysical Research*, *103*(B8), 17,885–17,899. https://doi.org/10.1029/98JB00904

Van Avendonk, H. J., Shillington, D. J., Holbrook, W. S., & Hornbach, M. J. (2004). Inferring crustal structure in the Aleutian island arc from a sparse wide-angle seismic data set. *Geochemistry, Geophysics, Geosystems*, *5*, Q08008. https://doi.org/10.1029/2003GC000664

van Keken, P. E., Hacker, B. R., Syracuse, E. M., & Abers, G. A. (2011). Subduction factory: 4. Depth-dependent flux of H_2O from subducting slabs worldwide. *Journal of Geophysical Research*, *116*, B01401. https://doi.org/10.1029/2010JB007922

Virieux, J. (1986). P-SV wave propagation in heterogeneous media: Velocity-stress finite-difference method. *Geophysics*, *51*(4), 889–901. https://doi.org/10.1190/1.1442147

Virieux, J., & Operto, S. (2009). An overview of full-waveform inversion in exploration geophysics. *Geophysics*, *74*(6), WCC1–WCC26. https://doi.org/10.1190/1.3238367

von Huene, R., & Lee, H. (1982). The possible significance of pore fluid pressures in subduction zones. *AAPG Memoir*, *34*, 781–791.

Wang, H., Singh, S. C., & Calandra, H. (2014). Integrated inversion using combined wave-equation tomography and full waveform inversion. *Geophysical Journal International*, *198*(1), 430–446. https://doi.org/10.1093/gji/ggu138

Wang, H., Singh, S. C., Audebert, F., & Calandra, H. (2015). Inversion of seismic refraction and reflection data for building long-wavelength velocity models. *Geophysics*, *80*(2), R81–R93. https://doi.org/10.3997/2214-4609. 20141088

Wells, R. E., Blakely, R. J., Sugiyama, Y., Scholl, D. W., & Dinterman, P. A. (2003). Basin-centered asperities in great subduction zone earthquakes: A link between slip, subsidence, and subduction erosion? *Journal of Geophysical Research*, *108*(B10), 2507. https://doi.org/10.1029/2002JB002072

Wiseman, K., Banerjee, P., Sieh, K., Bürgmann, R., & Natawidjaja, D. H. (2011). Another potential source of destructive earthquakes and tsunami offshore of Sumatra. *Geophysical Research Letters*, *38*, L10311. https://doi.org/10.1029/2011GL047226